

# Laminar and Turbulent Simulations of Several TVD Schemes in Two-Dimensions – Part I

EDISSON SÁVIO DE GÓES MACIEL  
Aeronautical Engineering Division (IEA)  
Aeronautical Technological Institute (ITA)

Pça. Mal. do Ar Eduardo Gomes, 50 – Vila das Acácias, 50 – São José dos Campos – SP – 12228-900  
BRAZIL

[edisavio@edissonsavio.eng.br](mailto:edisavio@edissonsavio.eng.br) <http://www.edissonsavio.eng.br>

*Abstract:* - This work, first of this study, describes five numerical tools to perform perfect gas simulations of the laminar and turbulent viscous flow in two-dimensions. The Van Leer, Harten, Frink, Parikh and Pirzadeh, Liou and Steffen Jr. and Radespiel and Kroll schemes, in their first- and second-order versions, are implemented to accomplish the numerical simulations. The Navier-Stokes equations, on a finite volume context and employing structured spatial discretization, are applied to solve the supersonic flow along a ramp in two-dimensions. Three turbulence models are applied to close the system, namely: Cebeci and Smith, Baldwin and Lomax and Sparlat and Allmaras. On the one hand, the second-order version of the Van Leer scheme is obtained from a “MUSCL” extrapolation procedure, whereas on the other hand, the second order version of the Harten scheme is obtained from the modified flux function approach. The convergence process is accelerated to the steady state condition through a spatially variable time step procedure, which has proved effective gains in terms of computational acceleration (see Maciel). The results have shown that, with the exception of the Harten scheme, all other schemes have yielded the best result in terms of the prediction of the shock angle at the ramp. Moreover, the wall pressure distribution is also better predicted by the Van Leer scheme.

*Key-Words:* - Laminar and turbulent flows, TVD algorithms, Cebeci and Smith turbulence model, Baldwin and Lomax turbulence model, Sparlat and Allmaras turbulence model.

## 1 Introduction

Conventional non-upwind algorithms have been used extensively to solve a wide variety of problems ([1]). Conventional algorithms are somewhat unreliable in the sense that for every different problem (and sometimes, every different case in the same class of problems) artificial dissipation terms must be specially tuned and judiciously chosen for convergence. Also, complex problems with shocks and steep compression and expansion gradients may defy solution altogether.

Upwind schemes are in general more robust but are also more involved in their derivation and application. Some upwind schemes that have been applied to the Euler equations are, for example, [2-5,7]. Some comments about these methods are reported below:

[2] developed a method suggesting an upwind scheme based on the flux vector splitting concept. This scheme considered the fact that the convective flux vector components could be written as flow Mach number polynomial functions, as main characteristic. Such polynomials presented the particularity of having the minor possible degree and the scheme had to satisfy seven basic properties to form such polynomials.

[3] developed a class of new finite difference schemes, explicit and with second order of spatial accuracy for calculation of weak solutions of the hyperbolic conservation laws. These highly nonlinear schemes were obtained by the application of a first order non-oscillatory scheme to an appropriately modified flux function. These second order algorithms reached high resolution, while preserving the robustness of the original scheme.

[4] proposed a new scheme, unstructured and upwind, to the solution of the Euler equations. They tested the precision and the utility of this scheme in the analysis of the inviscid flows around two airplane configurations: one of transport configuration, with turbines under the wings, and the other of high speed civil configuration. Tests were accomplished at subsonic and transonic Mach numbers with the transport airplane and at transonic and low supersonic Mach numbers with the civil airplane, yielding good results.

[5] proposed a new flux vector splitting scheme. They declared that their scheme was simple and its accuracy was equivalent and, in some cases, better than the [6] scheme accuracy in the solutions of the Euler and the Navier-Stokes equations. The scheme was robust and converged solutions were obtained

so fast as the [6] scheme. The authors proposed the approximated definition of an advection Mach number at the cell face, using its neighbour cell values via associated characteristic velocities. This interface Mach number was so used to determine the upwind extrapolation of the convective quantities.

[7] emphasized that the [5] scheme had its merits of low computational complexity and low numerical diffusion as compared to other methods. They also mentioned that the original method had several deficiencies. The method yielded local pressure oscillations in the shock wave proximities, adverse mesh and flow alignment problems. In the [7] work, a hybrid flux vector splitting scheme, which alternated between the [5] scheme and the [2] scheme, in the shock wave regions, was proposed, assuring that the resolution of strength shocks was clear and sharp.

Second order spatial accuracy can be achieved by introducing more upwind points or cells in the schemes. It has been noted that the projection stage, whereby the solution is projected in each cell face  $(i-1/2,j; i+1/2,j)$  on piecewise constant states, is the cause of the first order space accuracy of the Godunov schemes ([8]). Hence, it is sufficient to modify the first projection stage without modifying the Riemann solver, in order to generate higher spatial approximations. The state variables at the interfaces are thereby obtained from an extrapolation between neighboring cell averages. This method for the generation of second order upwind schemes based on variable extrapolation is often referred to in the literature as the MUSCL ("Monotone Upstream-centered Schemes for Conservation Laws") approach. The use of nonlinear limiters in such procedure, with the intention of restricting the amplitude of the gradients appearing in the solution, avoiding thus the formation of new extrema, allows that first order upwind schemes be transformed in TVD high resolution schemes with the appropriate definition of such nonlinear limiters, assuring monotone preserving and total variation diminishing methods.

Second order spatial accuracy can also be obtained from the use of a modified flux function approach, as suggested by [3]. This approach consists in adopting a modified flux to be considered in the numerical flux function. A limiter is used to consider only smooth variations of the flux function. Moreover, this minmod like limiter eliminates high variations of the flux function, reducing this one to a constant behaviour between the right and left states. This approach also introduces TVD like properties into the calculation algorithm.

Computational fluid dynamics (CFD) methods have been widely used in the design of aircraft. Because of the great difficulties in experimental study, CFD demonstrates its great importance in the simulation of transonic high-angle-of-attack (AOA) flow about realistic configurations, which is dominated by extremely complex phenomena such as shock/boundary-layer interaction, massive flow separation, and complicated vortex structures. Until now, numerical prediction of such phenomena has been highly dependent on the selection of turbulence models.

There is a practical necessity in the aeronautical industry and in other fields of the capability of calculating separated turbulent compressible flows. With the available numerical methods, researches seem able to analyze several separated flows, three-dimensional in general, if an appropriated turbulence model is employed. Simple methods as the algebraic turbulence models of [9-10] supply satisfactory results with low computational cost and allow that the main features of the turbulent flow be detected.

More elaborate treatments of turbulent flow, especially involving separation, are obtained with one-equation turbulence models. Such models are cheaper than their counterpart two-equation models and a bit more expensive than the algebraic models. One such a model is the [11] one. In this model, a transport equation for the turbulent viscosity is assembled, using empiricism and arguments of dimensional analysis, Galilean invariance and selective dependence on the molecular viscosity. The equation includes a destruction term that depends on the distance to the wall, related to the one in [12] model and to one due to [13]. Unlike early one-equation models, the resulting turbulence model is local (i.e., the equation at one point does not depend on the solution at others points) and therefore compatible with grids of any structure and Navier-Stokes solvers in two- and three-dimensions. It is numerically forgiving, in terms of near-wall resolution and stiffness, and yields rapid convergence to steady state.

In 2006, [14] have presented a work that considered first-order algorithms applied to the solution of an aerospace flow problem. The [3,7] algorithms, both first order accurate in space, were studied. The Navier-Stokes equations written in conservative form, employing a finite volume formulation and a structured spatial discretization, in two-dimensions, were solved. The [10] turbulence algebraic model closed the problem. The steady state physical problem of the supersonic flow around a simplified version of the VLS

configuration was studied. The results have demonstrated that the  $-C_p$  distribution around the geometry generated by the [3] scheme, in both solutions laminar and turbulent, was smoother than to the one obtained by the [7] scheme, presenting a minor pressure increase in the booster initial region. The lift and drag aerodynamic coefficients were minimized in the turbulent solution generated by the [3] scheme, presenting non-zero values. The [7] scheme predicted the same coefficients with values practically equal to zero to the laminar case and with small values in the turbulent case. The stagnation pressure ahead of the configuration was better predicted by the [3] scheme.

In 2008, [15] has presented a work, the second part of the study started in 2006, that considered upwind algorithms implemented with the [10] turbulence algebraic model applied to the solution of transonic and “cold gas” hypersonic problems. The [3,7] algorithms, both first order accurate in space, were studied. The Navier-Stokes equations written in conservative form, employing a finite volume formulation and a structured spatial discretization, in two-dimensions, were solved. The steady state physical problems of the transonic flow along a convergent-divergent nozzle and the “cold gas” hypersonic flow around a double ellipse configuration were studied. Results were compared with experimental or theoretical solutions. The results have shown good agreement between the tested algorithms. In the nozzle problem, the [3] scheme predicts a more severe shock at the throat than the [7] scheme, as well closer wall pressure distribution to experimental results, for both laminar and turbulent cases. In the double ellipse case, the [7] scheme presented more severe pressure field and better prediction of the stagnation pressure than the [3] scheme, again to both laminar and turbulent cases.

In 2010, [16] has presented a work that was the final part of the study that aimed a comparison between the turbulence models of [9] and [10] applied to aeronautical and aerospace problems. The [17] algorithm was used to perform the numerical experiments. The algorithm was symmetrical, second order accurate in space and time, and the temporal integration was accomplished by a Runge-Kutta type method. The Reynolds average Navier-Stokes equations were solved, using a finite volume formulation and a structured spatial discretization, and the models of [9] and [10] were used to describe the turbulence effects in the flow properties. The physical problems of the transonic flow along a convergent-divergent nozzle and the “cold gas” hypersonic flow around a double ellipse

configuration were studied. A spatially variable time step was employed to accelerate the convergence of the numerical scheme. Effective gains in terms of convergence ratio were observed with this technique, as reported in [18-19]. The numerical results were compared with experimental or theoretical solutions. These results have demonstrated that the [10] model was more severe in the nozzle problem, while the [9] model was more severe in the double ellipse problem and more accurate in both examples.

This work, first of this study, describes five numerical tools to perform perfect gas simulations of the laminar and turbulent viscous flow in two-dimensions. The [2-5,7] schemes, in its first- and second-order versions, are implemented to accomplish the numerical simulations. The Navier-Stokes equations, on a finite volume context and employing structured spatial discretization, are applied to solve the supersonic flow along a ramp in two-dimensions. Three turbulence models are applied to close the system, namely: [9], [10] and [11]. On the one hand, the second-order version of the [2,4-5,7] schemes are obtained from a “MUSCL” extrapolation procedure, whereas on the other hand, the modified flux function approach is applied in the [3] scheme for the same accuracy. The convergence process is accelerated to the steady state condition through a spatially variable time step procedure, which has proved effective gains in terms of computational acceleration (see [18-19]). The results have shown that the [2,4-5,7] schemes have yielded the best results in terms of the prediction of the shock angle at the ramp. Moreover, the wall pressure distribution is also better predicted by the [2] scheme.

## 2 Navier-Stokes Equations

The flow is modeled by the Navier-Stokes equations, which express the conservation of mass and energy as well as the momentum variation of a viscous, heat conducting and compressible media, in the absence of external forces. The integral and conservative form of these equations can be represented by:

$$\frac{\partial}{\partial t} \int_V Q dV + \int_S [(E_e - E_v)n_x + (F_e - F_v)n_y] dS = 0, \quad (1)$$

where  $Q$  is written for a Cartesian system,  $V$  is the cell volume,  $n_x$  and  $n_y$  are components of the normal versor to the flux face,  $S$  is the flux area,  $E_e$  and  $F_e$  are the components of the convective flux vector

and  $E_v$  and  $F_v$  are the components of the diffusive flux vector. The vectors  $Q$ ,  $E_e$ ,  $F_e$ ,  $E_v$  and  $F_v$  are represented by:

$$Q = \begin{Bmatrix} \rho \\ \rho u \\ \rho v \\ e \end{Bmatrix}, \quad E_e = \begin{Bmatrix} \rho u \\ \rho u^2 + p \\ \rho uv \\ (e+p)u \end{Bmatrix}, \quad F_e = \begin{Bmatrix} \rho v \\ \rho uv \\ \rho v^2 + p \\ (e+p)v \end{Bmatrix},$$

$$E_v = \frac{1}{Re} \begin{Bmatrix} 0 \\ \tau_{xx} \\ \tau_{xy} \\ \tau_{xx}u + \tau_{xy}v - q_x \end{Bmatrix}, \quad F_v = \frac{1}{Re} \begin{Bmatrix} 0 \\ \tau_{xy} \\ \tau_{yy} \\ \tau_{xy}u + \tau_{yy}v - q_y \end{Bmatrix}; \quad (2)$$

The components of the viscous stress tensor are defined as:

$$\tau_{xx} = 2\mu_{\text{effect}} \frac{\partial u}{\partial x} - \frac{2}{3}\mu_{\text{effect}} \left( \frac{\partial u}{\partial x} + \frac{\partial v}{\partial y} \right),$$

$$\tau_{xy} = \mu_{\text{effect}} \left( \frac{\partial u}{\partial y} + \frac{\partial v}{\partial x} \right),$$

$$\tau_{yy} = 2\mu_{\text{effect}} \frac{\partial v}{\partial y} - \frac{2}{3}\mu_{\text{effect}} \left( \frac{\partial u}{\partial x} + \frac{\partial v}{\partial y} \right); \quad (3)$$

and the components of the Fourier heat flux vector are defined as:

$$q_x = -\gamma \left( \frac{\mu}{Prd} \right)_{\text{effect}} \frac{\partial e_i}{\partial x}, \quad q_y = -\gamma \left( \frac{\mu}{Prd} \right)_{\text{effect}} \frac{\partial e_i}{\partial y}, \quad (4)$$

where  $\rho$  is the fluid density;  $u$  and  $v$  are the Cartesian components of velocity vector in the  $x$  and  $y$  directions, respectively;  $p$  is the static pressure;  $e$  is the total energy per unit volume; the  $\tau$ 's are the viscous stresses;  $q_x$  and  $q_y$  are the Cartesian components of the heat conduction vector (Fourier law);  $\gamma$  is the ratio of specific heats;  $\mu_{\text{effect}}$  is the effective fluid viscosity, which is equal to the sum of the molecular viscosity with the turbulent viscosity:

$$\mu_{\text{effect}} = \mu_M + \mu_T; \quad (5)$$

The  $(\mu/Prd)_{\text{effect}}$  is defined as:

$$(\mu/Prd)_{\text{effect}} = (\mu_M/Prd_L) + (\mu_T/Prd_T), \quad (6)$$

where  $Prd_L$  and  $Prd_T$  are the laminar and the turbulent Prandtl numbers, respectively, with  $Prd_L = 0,72$  and  $Prd_T = 0,9$ ;  $Re$  is the flow Reynolds number defined as:

$$Re = \rho u_{\text{REF}} l / \mu_M, \quad (7)$$

where  $u_{\text{REF}}$  is a characteristic flow speed and  $l$  is a characteristic configuration length; and the internal energy is given by:

$$e_i = e/\rho - 0.5(u^2 + v^2). \quad (8)$$

The molecular viscosity is estimated by the empiric Sutherland formula:

$$\mu_M = bT^{1/2} / (1 + S/T), \quad (9)$$

where  $T$  is the absolute temperature (K),  $b = 1.458 \times 10^{-6} \text{ Kg}/(\text{m.s.K}^{1/2})$  and  $S = 110.4 \text{ K}$ , to the atmospheric air in the standard atmospheric conditions ([20]).

The Navier-Stokes equations are dimensionless in relation to the freestream density, the freestream speed of sound and the freestream molecular viscosity. The system is closed by the state equation for a perfect gas:

$$p = (\gamma - 1) [e - 0.5\rho(u^2 + v^2)], \quad (10)$$

considering the ideal gas hypothesis. The total enthalpy is determined by:

$$H = (e + p)/\rho. \quad (11)$$

### 3 TVD Algorithms

The description of the convective algorithms of [2-5,7] is presented in [21-31] and the reader is encouraged to read these papers to become familiar with the numerical schemes. Moreover, the second order spatial accuracy, which incorporates TVD and high resolution properties, is described in [25-31]. Hereafter, this paper will present the viscous formulation of both numerical schemes.

The numerical flux vector is defined for the [3] scheme, for instance, considering the  $(i+1/2,j)$  interface:

$$F_{i+1/2,j}^l = \left( E_{e_{i+1/2,j}}^l - E_{v_{i+1/2,j}}^l \right) n_x + \left( F_{e_{i+1/2,j}}^l - F_{v_{i+1/2,j}}^l \right) n_y + 0.5D_{\text{Harter}}^l \quad (12)$$

where:  $l$  varies from 1 to 4 (two-dimensional space) and  $D_{Harten}$  is the Harten's dissipation function, defined in [23-26]. The Euler vectors are defined by the convective contributions of the numerical schemes.

The viscous vectors are calculated with the gradients of the conserved and primitive variables keeping constant in each volume and the application of the Green's theorem to change from a volume integral to a surface integral.

The time integration is performed by a time splitting method, for the [2-3,5,7] schemes, which divides the integration in two parts, each one associated with a spatial coordinate direction. Therefore, to the  $\xi$  direction, one has:

$$\begin{aligned} \Delta Q_{i,j}^* &= -\frac{\Delta t_{i,j}}{V_{i,j}} (F_{i+1/2,j}^n - F_{i-1/2,j}^n); \\ Q_{i,j}^* &= Q_{i,j}^n + \Delta Q_{i,j}^*; \end{aligned} \quad (13)$$

and to the  $\eta$  direction, one has:

$$\begin{aligned} \Delta Q_{i,j}^{n+1} &= -\frac{\Delta t_{i,j}}{V_{i,j}} (F_{i,j+1/2}^* - F_{i,j-1/2}^*); \\ Q_{i,j}^{n+1} &= Q_{i,j}^* + \Delta Q_{i,j}^{n+1}. \end{aligned} \quad (14)$$

The [4] scheme uses a Runge-Kutta time stepping method to perform time integration. This Runge-Kutta method is a five step one. Details in [30-31].

## 4 Turbulence Models

### 4.1 Turbulence model of Cebeci and Smith

The problem of the turbulent simulation is in the calculation of the Reynolds stress. Expressions involving velocity fluctuations, originating from the average process, represent six new unknowns. However, the number of equations keeps the same and the system is not closed. The modeling function is to develop approximations to these correlations. To the calculation of the turbulent viscosity according to the [9] model, the boundary layer is divided in internal and external.

Initially, the ( $\nu_w$ ) kinematic viscosity at wall and the ( $\tau_{xy,w}$ ) shear stress at wall are calculated. After that, the ( $\delta$ ) boundary layer thickness, the ( $\delta_{LM}$ ) linear momentum thickness and the ( $V_{tBL}$ ) boundary layer tangential velocity are calculated. So, the ( $N$ ) normal distance from the wall to the studied cell is calculated. The  $N^+$  term is obtained from:

$$N^+ = \sqrt{Re} \sqrt{\tau_{xy,w} / \rho_w} N / \nu_w, \quad (15)$$

where  $\rho_w$  is the wall density. The van Driest damping factor is calculated by:

$$D = 1 - e^{(-N^+ \sqrt{\rho/\rho_w} \mu_w / \mu / A^+)}, \quad (16)$$

with  $A^+ = 26$  and  $\mu_w$  is the wall molecular viscosity. After that, the ( $dVt/dN$ ) normal to the wall gradient of the tangential velocity is calculated and the internal turbulent viscosity is given by:

$$\mu_{Ti} = Re \rho (\kappa N D)^2 dVt/dN, \quad (17)$$

where  $\kappa$  is the von Kármán constant, which has the value 0.4. The intermittent function of Klebanoff is calculated to the external viscosity by:

$$g_{Kleb}(N) = [1 + 5.5(N/\delta)^6]^{-1}. \quad (18)$$

With it, the external turbulent viscosity is calculated by:

$$\mu_{Te} = Re(0.0168) \rho Vt_{BL} \delta_{LM} g_{Kleb}. \quad (19)$$

Finally, the turbulent viscosity is chosen from the internal and the external viscosities:  $\mu_T = \text{MIN}(\mu_{Ti}, \mu_{Te})$ .

### 4.2 Turbulence model of Baldwin and Lomax

To the calculation of the turbulent viscosity according to the [10] model, the boundary layer is again divided in internal and external. In the internal layer,

$$\mu_{Ti} = \rho l_{mix}^2 \|\omega\| \quad \text{and} \quad l_{mix} = \kappa N \left(1 - e^{-N^+/A_0^+}\right). \quad (20)$$

In the external layer,

$$\mu_{Te} = \rho \alpha C_{cp} F_{wake} F_{Kleb}(N; N_{max} / C_{Kleb}), \quad (21)$$

with:

$$F_{wake} = \text{MIN} \left[ N_{max} F_{max}; C_{wk} N_{max} U_{dif}^2 / F_{max} \right], \quad (22a)$$

$$F_{max} = 1/\kappa \left[ \text{MAX}_N (l_{mix} \|\omega\|) \right]. \quad (22b)$$

Hence,  $N_{max}$  is the value of  $N$  where  $l_{mix} \|\omega\|$  reached its maximum value and  $l_{mix}$  is the Prandtl

mixture length. The constant values are:  $\kappa = 0.4$ ,  $\alpha = 0.0168$ ,  $A_0^+ = 26$ ,  $C_{cp} = 1.6$ ,  $C_{Kleb} = 0.3$  and  $C_{wk} = 1$ .  $F_{Kleb}$  is the intermittent function of Klebanoff given by:

$$F_{Kleb}(N) = \left[ 1 + 5.5(C_{Kleb} N/N_{max})^6 \right]^{-1}, \quad (23)$$

$\|\omega\|$  is the magnitude of the vortex vector and  $U_{dif}$  is the maximum velocity value in the boundary layer case. To free shear layers,

$$U_{dif} = \left( \sqrt{u^2 + v^2 + w^2} \right)_{max} - \left( \sqrt{u^2 + v^2 + w^2} \right)_{N=N_{max}}. \quad (24)$$

### 4.3 Turbulence model of Sparlat and Allmaras

The purpose of the [11] one-equation model was overcome the algebraic model limitations and, at the same time, to avoid the difficulties in the implementation of the two-equation models or the Reynolds stress equations. This model employs a transport turbulent viscosity to solve the turbulence scaling. Such model takes naturally into account the turbulence and diffusion histories, which improves its accuracy.

The transport equation to the work turbulent kinematic viscosity is described by:

$$\frac{D\tilde{\nu}}{Dt} = c_{b1}\tilde{S}\tilde{\nu} + \frac{1}{\sigma} \left[ \nabla \cdot ((v + \tilde{\nu})\nabla\tilde{\nu}) + c_{b2}(\nabla\tilde{\nu})^2 \right] - c_{w1}f_w(r) \left( \frac{\tilde{\nu}}{N} \right)^2. \quad (25)$$

In this equation, the first term of the right-hand-side is the production contribution to the work kinematic viscosity; the second term is the viscosity diffusion; and the last term is the destruction of the work kinematic viscosity. The turbulent viscosity is defined by:

$$\mu_T = \rho\tilde{\nu}f_{v1}. \quad (26)$$

With the purpose of assuring that  $\tilde{\nu}$  becomes equal to  $K \times N \times \sqrt{\tau_{xy,w}/\rho_w}$  in the logarithmic layer and in the viscous sub-layer, the  $f_{v1}$  damping function is defined by:

$$f_{v1} = \frac{\lambda^3}{\lambda^3 + c_{v1}^3} \quad (27)$$

as function of the  $\lambda = \tilde{\nu}/\nu$  variable. The  $\tilde{S}$  function, representing the deformation work of the mean flow, is determined as follows:

$$\tilde{S} = \left| \frac{\partial u}{\partial y} \right| + \left[ \frac{\tilde{\nu}}{(\kappa N)^2} f_{v2} \right], \quad (28)$$

in which  $f_{v2}$  has the following expression:

$$f_{v2} = 1 - \frac{\lambda}{1 + \lambda f_{v1}}. \quad (29)$$

The destruction term should disappear at the external region of the boundary layer. [11] purpose the following function to reproduce such behaviour:

$$f_w(r) = g \left[ \frac{1 + c_{w3}^6}{g^6 + c_{w3}^6} \right]^{1/6}, \quad g = r + c_{w2}(r^6 - r);$$

$$r = \frac{\tilde{\nu}}{(\kappa N)^2 \tilde{S}}, \quad (30)$$

with the  $r$  argument and the  $f_w$  function reaching the value 1.0 at the logarithmic layer and decreasing at the external region. The  $g$  function is merely a limiter to prevent  $f_w$  high values. The [11] model constants are:

$$c_{b1} = 0,1355, \quad c_{b2} = 0,622, \quad c_{w2} = 0,3, \quad c_{v1} = 7,1;$$

$$\sigma = 2/3, \quad c_{w3} = 2,0, \quad c_{w1} = \frac{c_{b1}}{\kappa^2} + \frac{(1 + c_{b2})}{\sigma}. \quad (31)$$

The [11] model is marched in time using a LU-SGS (“Lower-Upper Factorization – Symmetrical Gauss-Seidel”) implicit method. Details of the implicit implementation in two-dimensions are found in [11]. The extension to three-dimensions is straightforward.

In this work, the term referent to the diffusion of the work kinematic viscosity was not implemented. The studied model considers only the production and dissipation terms of the work kinematic viscosity.

## 5. Spatially Variable Time Step

The basic idea of the spatially variable time step procedure consists in keeping constant the CFL number in all calculation domain, allowing, hence, the use of appropriated time steps to each specific mesh region during the convergence process. In this

work, a convective + diffusive option of spatially variable time step calculated at each iteration was studied and is described below:

To a viscous simulation and according to the work of [32], it is possible to write:

$$\Delta t_i = \left( \frac{\text{CFL}(\Delta t_c \Delta t_v)}{\Delta t_c + \Delta t_v} \right)_{i,j}, \quad (32)$$

with  $\Delta t_c$  being the convective time step and  $\Delta t_v$  being the viscous time step. These quantities are defined as:

$$\begin{aligned} (\Delta t_c)_{i,j} &= \frac{V_{i,j}}{(\lambda_c)_{i,j}}; \\ (\lambda_c)_{i,j} &= \max(\lambda_{i,j-1/2}^{\max}, \lambda_{i+1/2,j}^{\max}, \lambda_{i,j+1/2}^{\max}, \lambda_{i-1/2,j}^{\max}); \\ \lambda_{\text{int}}^{\max} &= \left( \mathbf{u}_{\text{int}} \mathbf{n}_x + \mathbf{v}_{\text{int}} \mathbf{n}_y \right) + \mathbf{a}_{\text{int}} \mathbf{S}_{\text{int}}; \quad (33) \\ (\Delta t_v)_{i,j} &= K_v \frac{V_{i,j}}{(\lambda_v)_{i,j}}, \quad (p1)_{i,j} = \frac{\gamma^{3/2} M_\infty}{(\text{RePrd}_L) V_{i,j}}; \\ (p2)_{i,j} &= \frac{\mu_{i,j-1/2}}{\rho_{i,j-1/2}} S_{i,j-1/2}^2 + \frac{\mu_{i+1/2,j}}{\rho_{i+1/2,j}} S_{i+1/2,j}^2 + \frac{\mu_{i,j+1/2}}{\rho_{i,j+1/2}} S_{i,j+1/2}^2 + \\ &\frac{\mu_{i-1/2,j}}{\rho_{i-1/2,j}} S_{i-1/2,j}^2; \quad (\lambda_v)_{i,j} = (p1 \times p2)_{i,j}, \quad (34) \end{aligned}$$

where interface properties are calculated by arithmetical average,  $M_\infty$  is the freestream Mach number,  $\mu$  is the fluid molecular viscosity and  $K_v$  is equal to 0.25, as recommended by [32].

## 6. Initial and Boundary Conditions

### 6.1 Initial Condition

Freestream values, at all grid cells, are adopted for all flow properties as initial condition, as suggested by [17] and [33]. Therefore, the vector of conserved variables is defined as:

$$Q_{i,j} = \left\{ 1 \quad M_\infty \cos \alpha \quad M_\infty \sin \alpha \quad \frac{1}{\gamma(\gamma-1)} + 0.5M_\infty^2 \right\}^T. \quad (35)$$

### 6.2 Boundary Conditions

The boundary conditions are basically of three types: solid wall, entrance, and exit. These conditions are implemented in ghost cells.

#### 6.2.1 Wall Condition

Considering the viscous case, it imposes the non-permeability and non-slip wall conditions. Therefore, the tangent velocity component of the ghost volume at wall has the same magnitude as the respective velocity component of its real neighbor cell, but opposite signal. In the same way, the normal velocity component of the ghost volume at wall is equal in value, but opposite in signal, to the respective velocity component of its real neighbor cell. These procedures lead to the following expressions to  $u_{\text{ghost}}$  and  $v_{\text{ghost}}$ :

$$\begin{aligned} u_{\text{ghost}} &= -u_{\text{real}} \\ v_{\text{ghost}} &= -v_{\text{real}} \end{aligned} \quad (36)$$

The pressure gradient normal to the wall is assumed to be equal to zero, following a boundary-layer like condition. The same hypothesis is applied to the temperature gradient normal to the wall, considering adiabatic wall. The ghost volume density and pressure are extrapolated from the respective values of the real neighbor volume (zero order extrapolation), with these two conditions. The total energy is obtained by the state equation of a perfect gas.

#### 6.2.2 Entrance Condition

The entrance condition considers subsonic and supersonic flow. They are detailed below:

(a) Subsonic flow: Three properties are specified and one extrapolated. This approach is based on information propagation analysis along characteristic directions in the calculation domain (see [33]). In other words, for subsonic flow, three characteristic propagate information point into the computational domain. Thus three flow properties must be fixed at the inlet plane. Just one characteristic line allows information to travel upstream. So, one flow variable must be extrapolated from the grid interior to the inlet boundary. The pressure was the extrapolated variable from the real neighbor volumes, for the studied problem. Density and velocity components adopted values of freestream flow.

(b) Supersonic flow: In this case no information travels upstream; therefore all variables are fixed with their freestream values.

#### 6.2.3 Exit Condition

Again, two flow situations are analyzed. They are detailed below:

(a) Subsonic flow: Three characteristic propagate information outward the computational domain. Hence, the associated variables should be extrapolated from interior information. The characteristic direction associated to the “ $(q_{normal-a})$ ” velocity should be specified because it point inward to the computational domain (see [33]). In this case, the ghost volume pressure is specified from its initial value. Density, and velocity components are extrapolated. The total energy is obtained from the state equation of a perfect gas.

(b) Supersonic flow: All variables are extrapolated from interior grid cells, as no flow information can make its way upstream. In other words, nothing can be fixed.

### 7. Results

One problem was studied in this work, namely: the viscous supersonic flow along a ramp geometry. The ramp configuration is detailed as also the type of boundary contours. These configuration characteristics are described in Figs. 1 and 2.

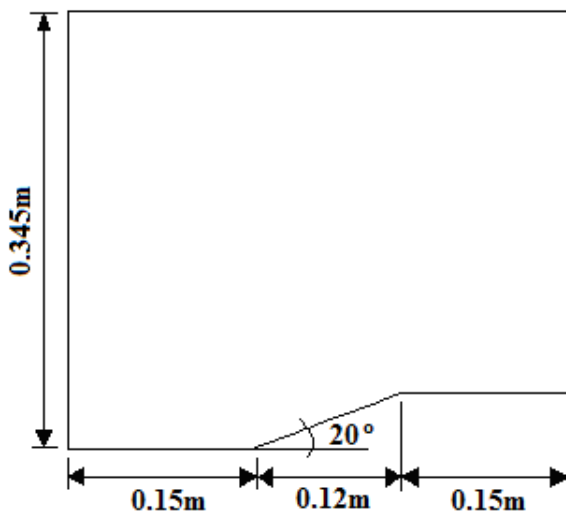


Figure 1. Ramp Configuration.

Numerical experiments were run on a Notebook computer with Intel Core i7 processor of 2.3GHz of clock and 8.0 GBytes of RAM. The criterion adopted to reach the steady state was to consider a reduction of three (3) orders of magnitude in the value of the maximum residual in the calculation domain, a typical CFD community criterion. The maximum residual is defined as the maximum value obtained from the discretized equations in the overall domain, considering all conservation equations.

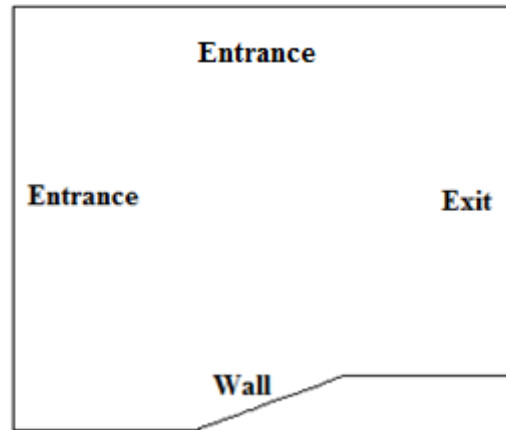


Figure 2. Ramp Computational Domain.

The initial conditions to the ramp problem are described in Tab. 1.

Table 1. Initial Conditions to the Studied Problem.

| Problem: | Property:                         | Value: |
|----------|-----------------------------------|--------|
| Ramp     | Freestream Mach, $M_\infty$       | 2.0    |
|          | Attack angle, $^\circ$            | 0.0    |
|          | Ratio of specific heats, $\gamma$ | 1.4    |

The number of cells and nodes for the ramp problem are presented in Tab. 2. A mesh of 61x60 nodes, in a finite difference context, is employed.

Table 2. Cells and Nodes of the Mesh.

| Problem: | Number of rectangular cells: | Number of nodes: |
|----------|------------------------------|------------------|
| Ramp     | 3,540                        | 3,660            |

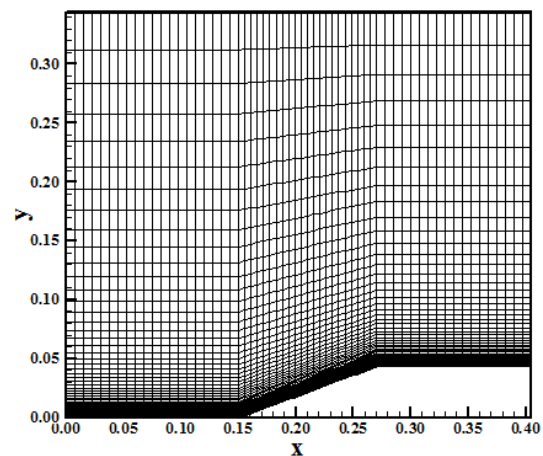


Figure 3. Ramp viscous mesh.

Figure 3 exhibits the mesh employed in the calculation of the viscous flow to the ramp problem.



An exponential stretching of 10.0% was applied close to the wall, in the  $\eta$  direction, to capture the viscous phenomena.

The Reynolds number is equal to  $1.613 \times 10^5$ , a turbulent flow. Three turbulence models will be studied, namely: [9-11]. Two algebraic and an one-equation models are implemented.

### 7.1 Laminar Viscous Results

The laminar viscous results are divided in two solution groups: the first order and the second order solutions. The first order results are presented here to serve as a benchmark to compare the second order viscous results, aiming to distinguish the excessive diffusion characteristics resulting from the former, as referenced by the CFD literature.

#### 7.1.1 First order results

Figures 4 to 8 presents the pressure contours obtained by the [2-5,7] schemes, respectively. All schemes capture a strong viscous interaction typical of viscous flow simulations, at the ramp entrance.

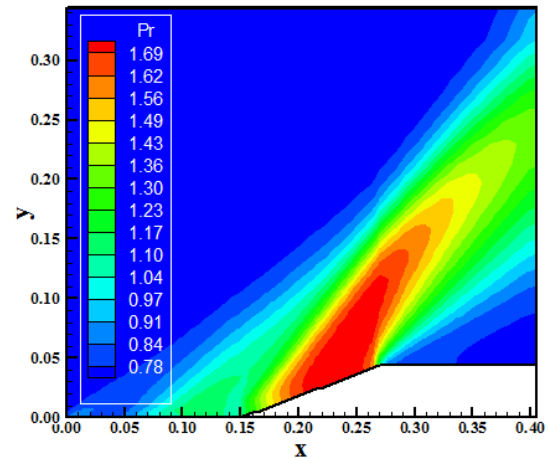


Figure 6. Pressure contours (FPP-1<sup>st</sup> Order).

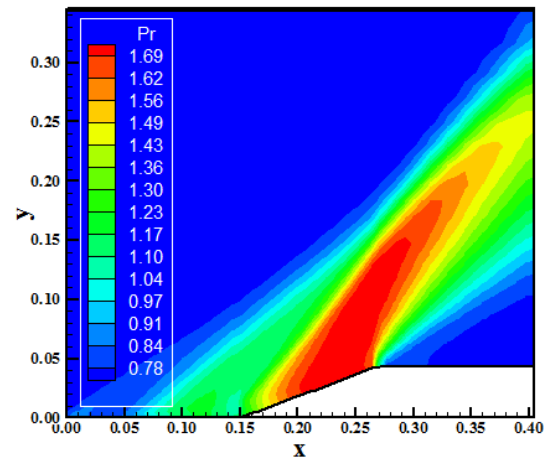


Figure 7. Pressure contours (LS-1<sup>st</sup> Order).

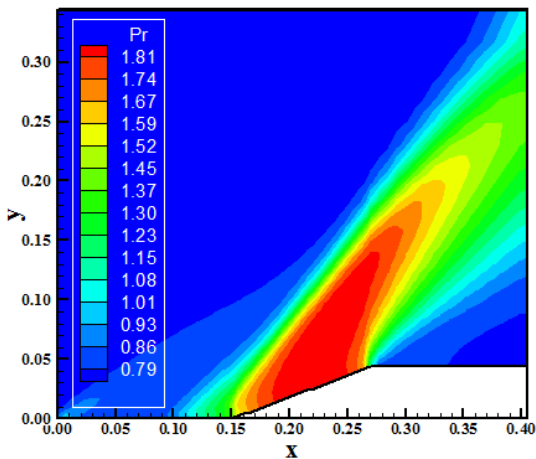


Figure 4. Pressure contours (VL-1<sup>st</sup> Order).

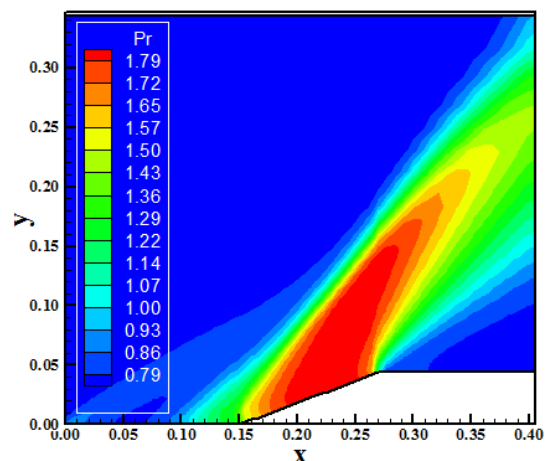


Figure 8. Pressure contours (RK-1<sup>st</sup> Order).

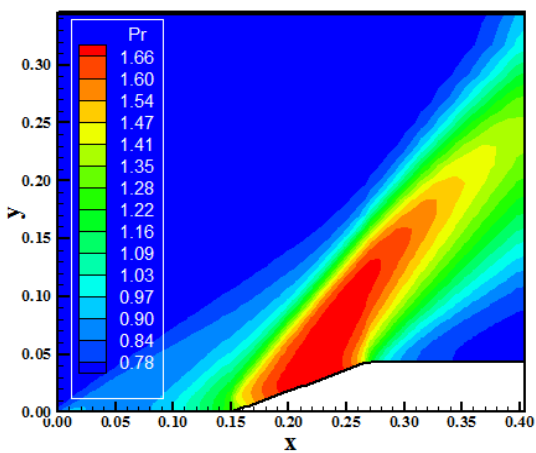


Figure 5. Pressure contours (H-1<sup>st</sup> Order).

A weak shock wave is formed ahead of the ramp due to the boundary layer detachment. The [3] scheme captures the biggest detachment region of the boundary layer, resulting in the biggest

circulation bubble formation. Moreover, the [2] scheme captures the most severe pressure field, characterizing this one as more conservative than the others schemes.

Figures 9 to 13 exhibit the Mach number contours obtained by the [2-5,7] schemes, respectively. All schemes capture the boundary layer detachment close to the ramp corner. Apparently, the all schemes capture the same region of separation flow and consequently the same bubble size. The five fields are approximately the same in quantitative terms.

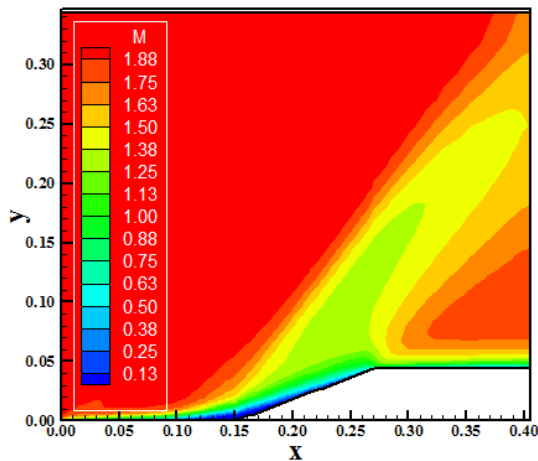


Figure 9. Mach number contours (VL-1<sup>st</sup> Order).

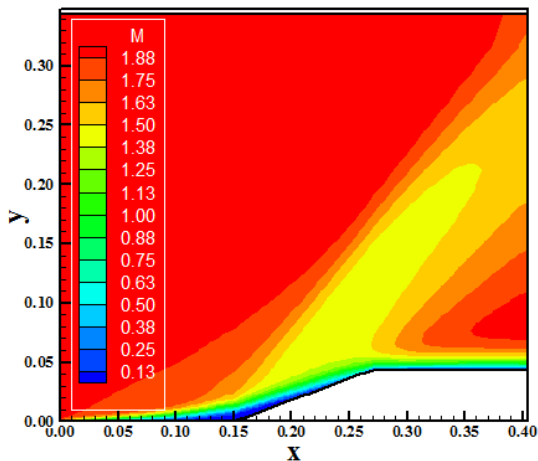


Figure 10. Mach number contours (H-1<sup>st</sup> Order).

Figure 14 presents the wall pressure distributions of all schemes. They are compared with the oblique shock wave theory results and with the Prandtl-Meyer expansion fan results. It is important to observe that this theoretical profile is the correct to be obtained in a viscous simulation, because of the pressure gradient in the normal direction from the wall is equal to zero, according to the boundary

layer theory. Hence, the pressure at the boundary layer edge is imposed to the wall pressure.

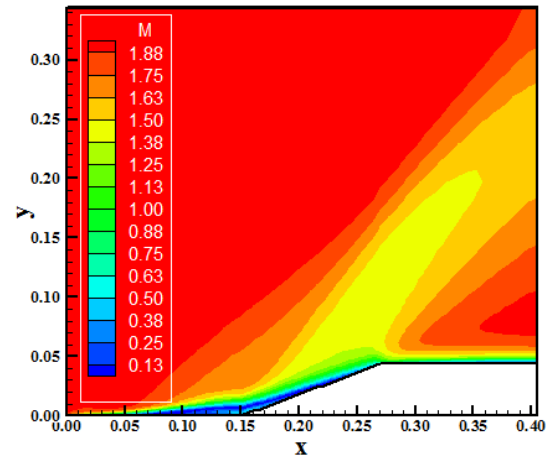


Figure 11. Mach number contours (FPP-1<sup>st</sup> Order).

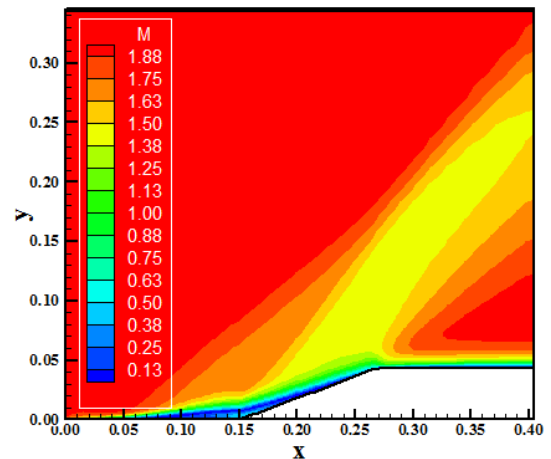


Figure 12. Mach number contours (LS-1<sup>st</sup> Order).

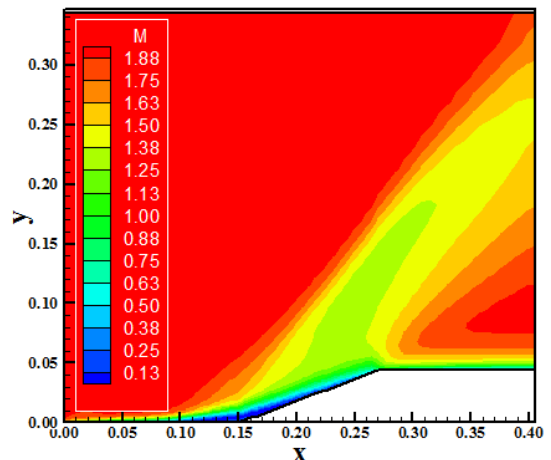


Figure 13. Mach number contours (RK-1<sup>st</sup> Order).

As can be seen, the [2] solution is closer to the pressure profile than the other solutions. The [3]

scheme predicted the smallest severe shock than the others schemes. The expansion fan is better captured by the [5] scheme.

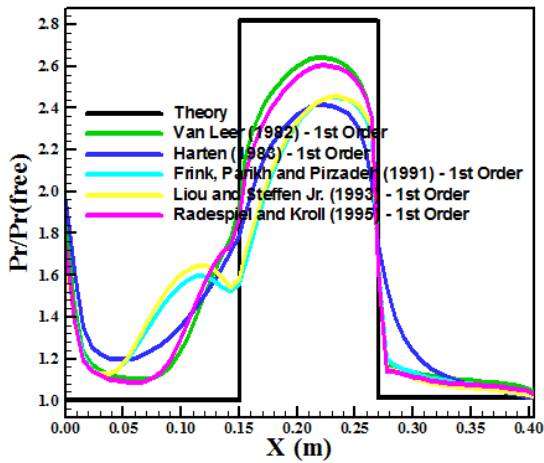


Figure 14. Wall pressure distributions.

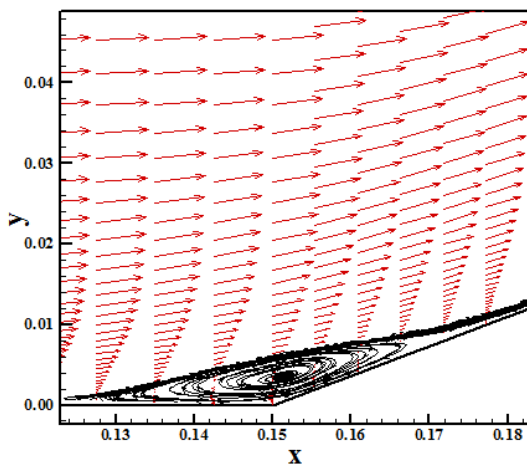


Figure 15. Circulation bubble. (VL-1<sup>st</sup> Order).

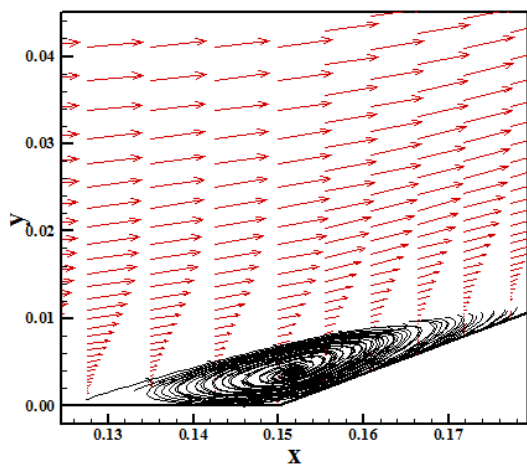


Figure 16. Circulation bubble. (H-1<sup>st</sup> Order).

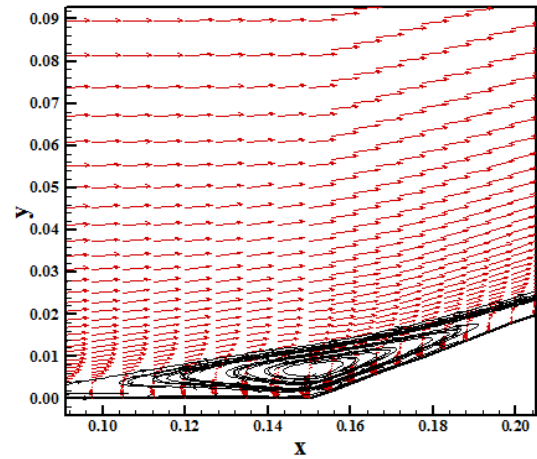


Figure 17. Circulation bubble (FPP-1<sup>st</sup> Order).

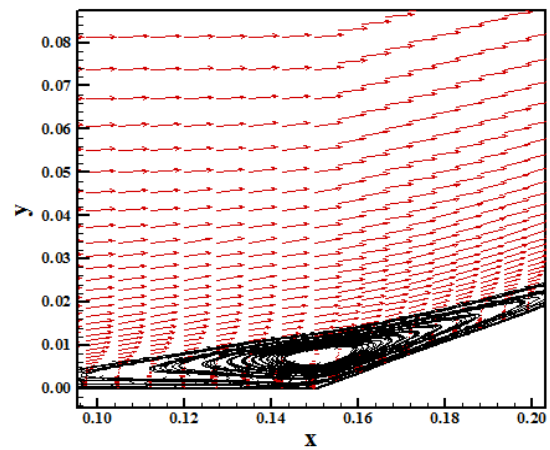


Figure 18. Circulation bubble (LS-1<sup>st</sup> Order).

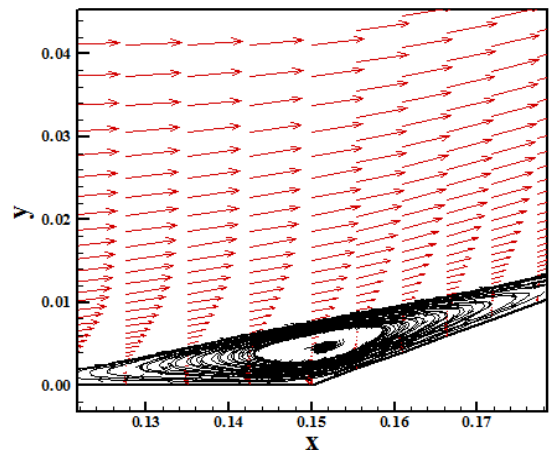


Figure 19. Circulation bubble (RK-1<sup>st</sup> Order).

Finally, the circulation bubble closes to the ramp corner is exhibited in Figs. 15 to 19. The [4-5] solutions show bigger circulation bubbles than the other solutions.

**7.1.2 Second order results/TVD**

For the second order results, a minmod non-linear limiter was employed in the [2,4-5,7] scheme. The [5,7] schemes did not present converged results. Figures 20 to 22 exhibit the pressure contours obtained by the [2-4] schemes.

All solutions present a weak shock ahead of the ramp corner. This shock wave is formed far ahead the ramp corner. The pressure field is also more severe in the solution obtained by the [2] scheme, indicating this one as the most conservative.

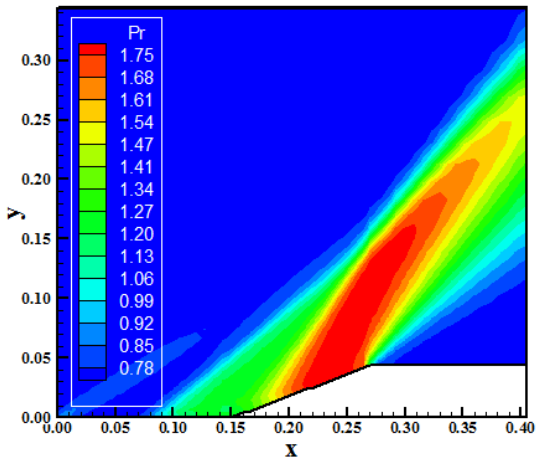


Figure 20. Pressure contours (VL-TVD).

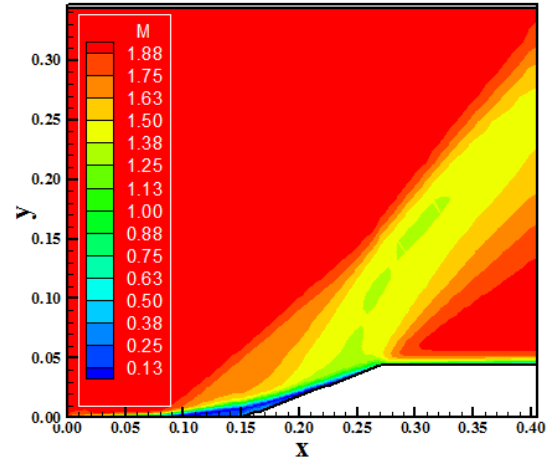


Figure 23. Mach number contours (VL-TVD).

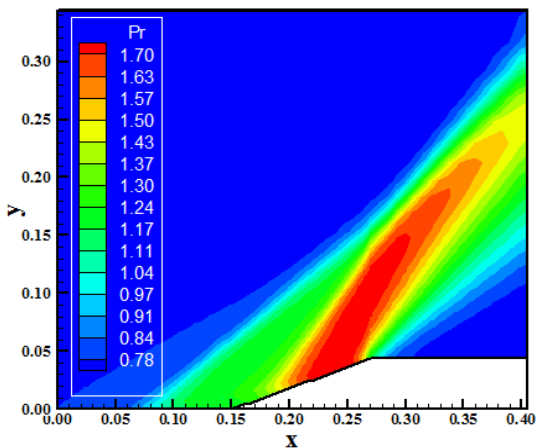


Figure 21. Pressure contours (H-TVD).

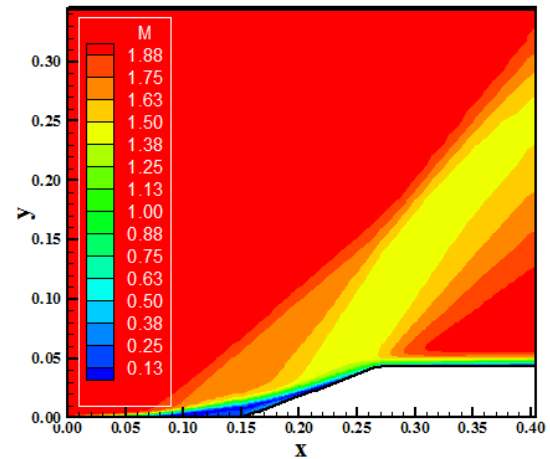


Figure 24. Mach number contours (H-TVD).

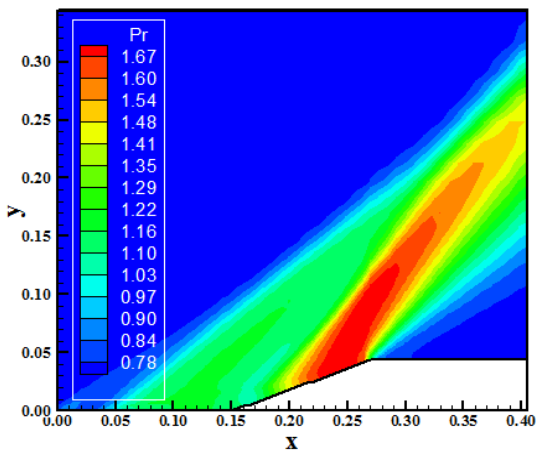


Figure 22. Pressure contours (FPP-TVD).

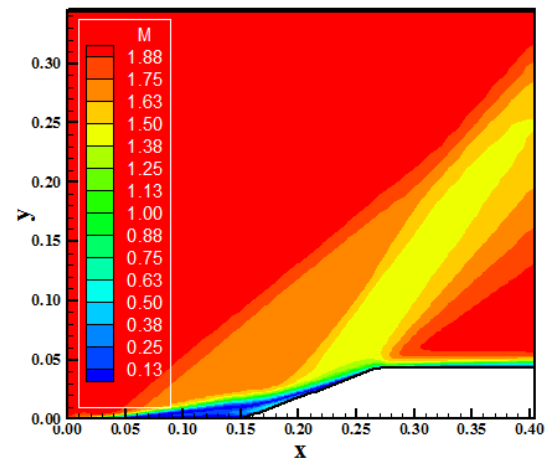


Figure 25. Mach number contours (FPP-TVD).

Figures 23 to 25 show the Mach number contours obtained by the [2-4] algorithms. All solutions present a significant region of the detached boundary layer. No quantitative differences exists in the solutions, although in qualitative terms the [2] solution is more correct.

Figure 26 shows the wall pressure distributions generated by the [2-4] schemes in their TVD versions. All solutions capture the circulation bubble formation, resulting from the boundary layer detachment. The [2] solution presents a pressure distribution closer to the pressure plateau, whereas the [4] solution shows a more extent separation region.

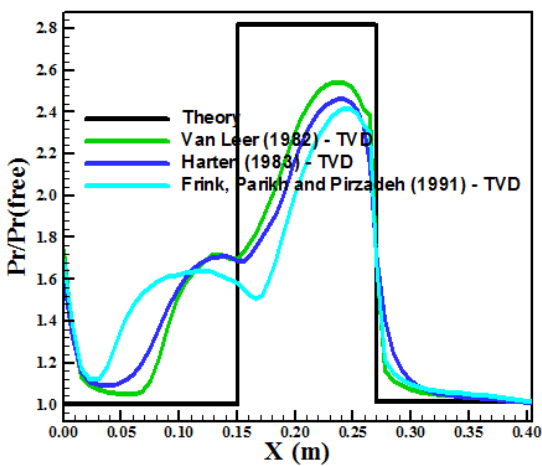


Figure 26. Wall pressure distributions.

Figures 27 to 29 presents the formation of circulation bubble closes to the ramp corner obtained by [2-4] schemes. The circulation bubbles obtained by the [3-4] schemes are larger than the respective of the [2] scheme.

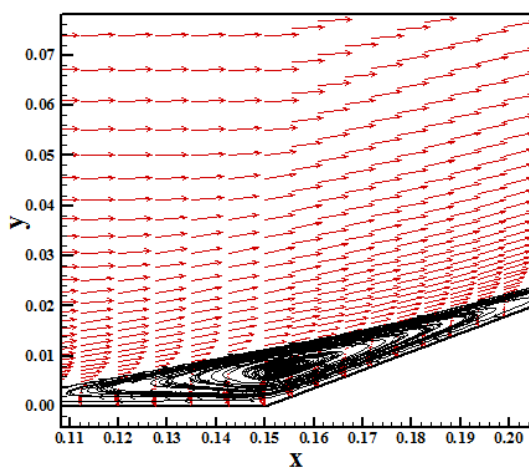


Figure 27. Circulation bubble (VL-TVD).

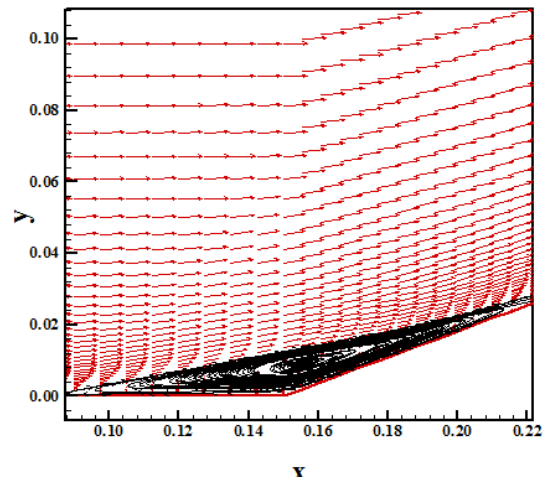


Figure 28. Circulation bubble (H-TVD).

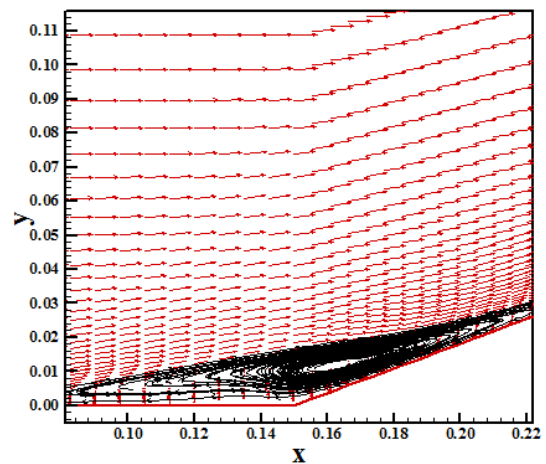


Figure 29. Circulation bubble (FPP-TVD).

As a resume of the present simulations, the [2] scheme was more conservative and more correct in physical terms, representing accurately the flow physics.

## 7.2 Turbulent Viscous Results

### 7.2.1 Cebeci and Smith results/TVD

Figures 30 to 34 show the pressure contours obtained by the [2-5,7] schemes, respectively, as using the [9] turbulence model. All solutions practically ignore the existence of the weak shock ahead of the ramp corner. It indicates that the boundary layer detachment is negligible in all solutions and that the circulation bubble is reduced in size. The pressure field generated by the [3] scheme is the most severe in relation to those generated by the other schemes.

Figures 35 to 39 exhibit the Mach number contours generated by the [2-5,7] numerical

algorithms, as using the [9] turbulence model. As can be observed, the boundary layer detachment is reduced in relation to the other results aforementioned for all algorithms. The circulation bubble is much more reduced.

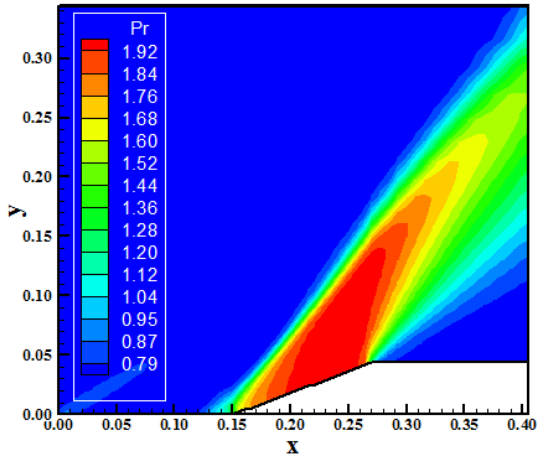


Figure 30. Pressure contours (Roe-CS).

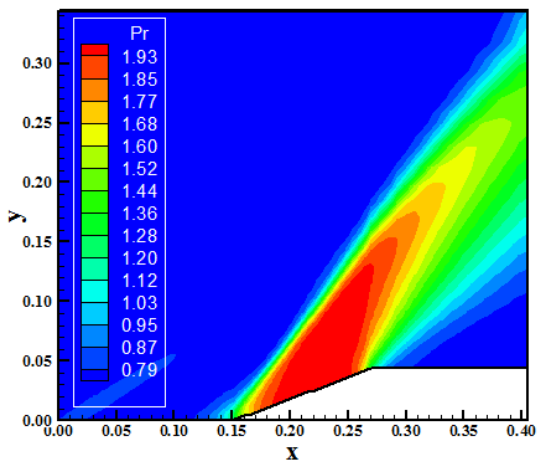


Figure 31. Pressure contours (H-CS).

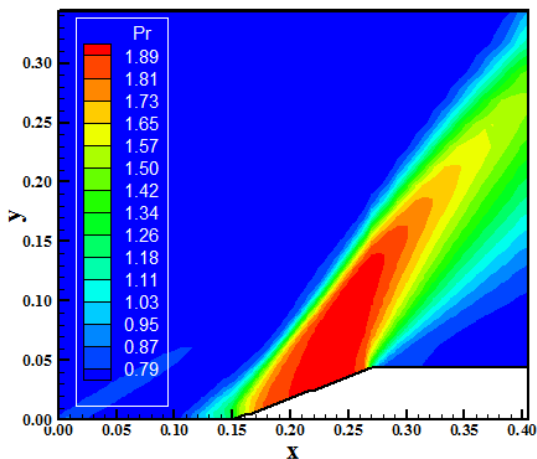


Figure 32. Pressure contours (FPP-CS).

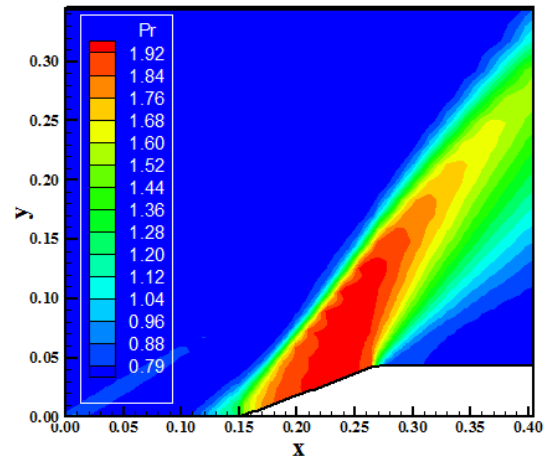


Figure 33. Pressure contours (LS-CS).

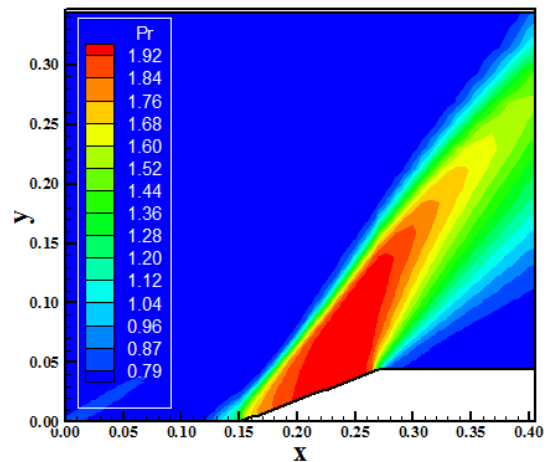


Figure 34. Pressure contours (RK-CS).

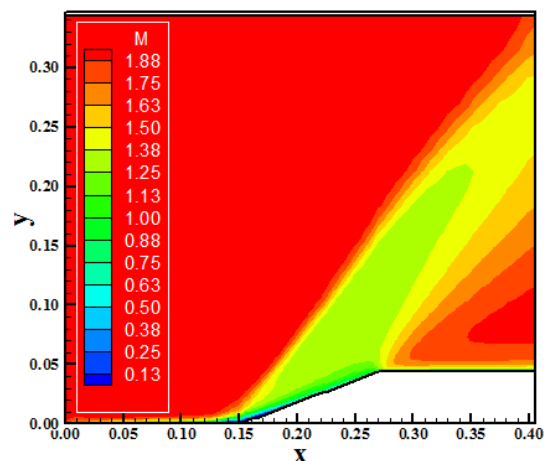


Figure 35. Mach number contours (VL-CS).

Figure 40 exhibits the wall pressure distributions obtained by the [2-5,7] algorithms, as using the [9] turbulence model. As can be observed, all solutions are very similar and agree better with the theoretical

solution than in the laminar cases. The expansion fan pressure is better predicted by the [7] algorithm.

predicted a small circulation bubble, although that generated by the [2] scheme is larger than those generated by the other schemes.

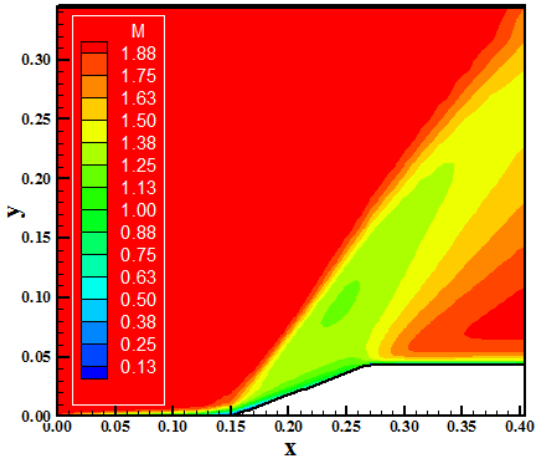


Figure 36. Mach number contours (H-CS).

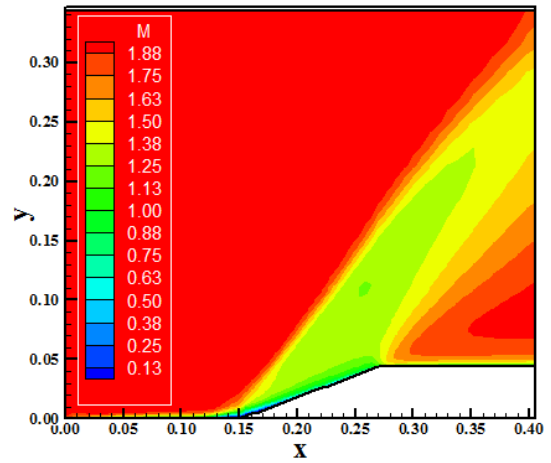


Figure 39. Mach number contours (RK-CS).

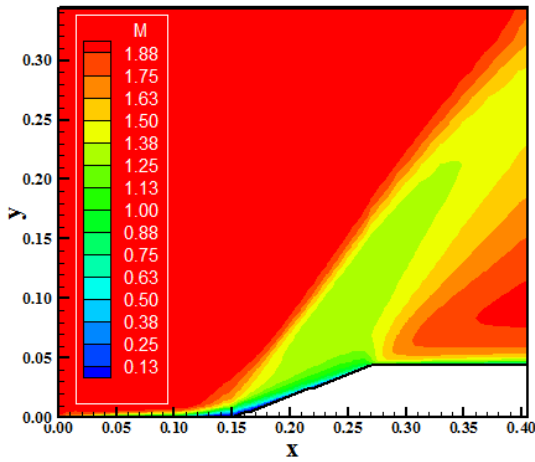


Figure 37. Mach number contours (FPP-CS).

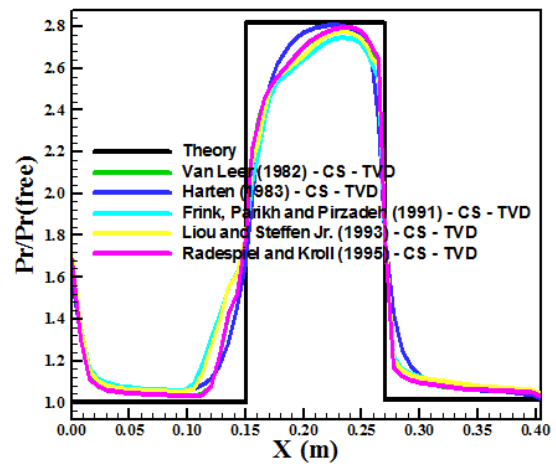


Figure 40. Wall pressure distributions.

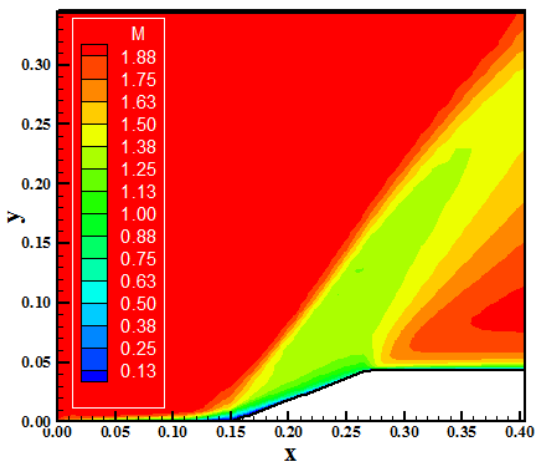


Figure 38. Mach number contours (LS-CS).

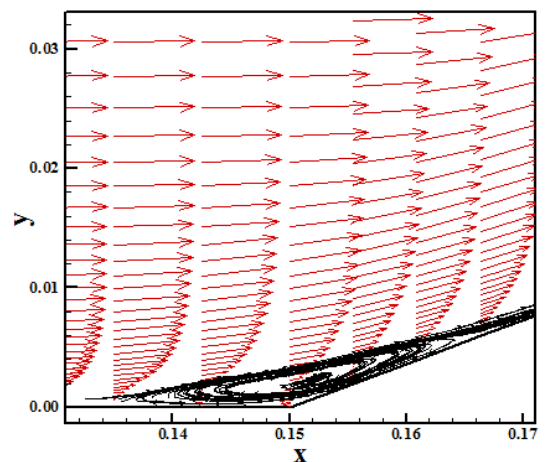


Figure 41. Circulation bubble (VL-CS).

Figures 41 to 45 show the circulation bubble formation close to the ramp corner. All solutions

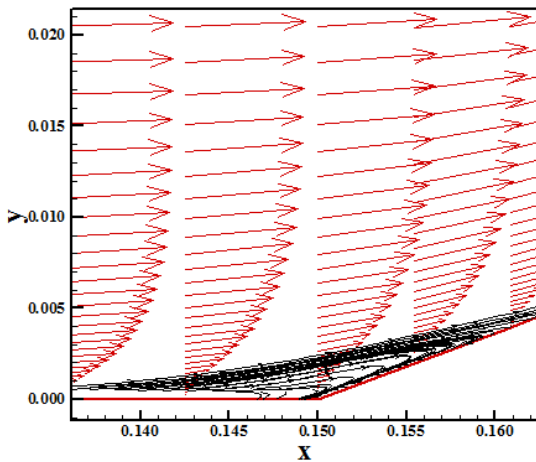


Figure 42. Circulation bubble (H-CS).

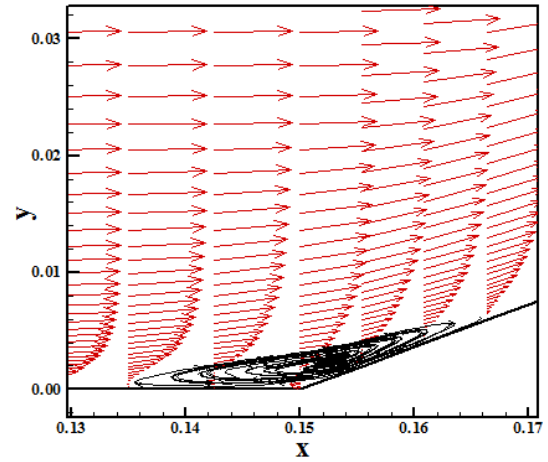


Figure 45. Circulation bubble (RK-CS).

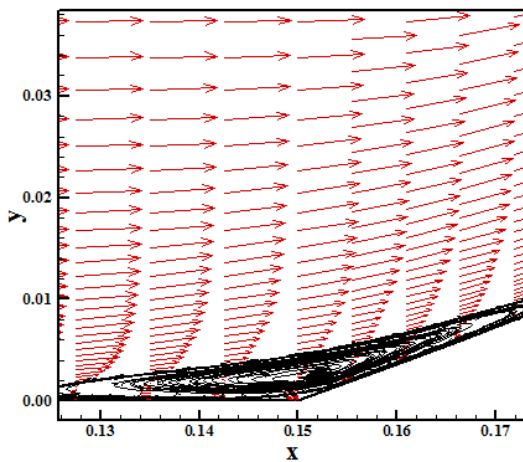


Figure 43. Circulation bubble (FPP-CS).

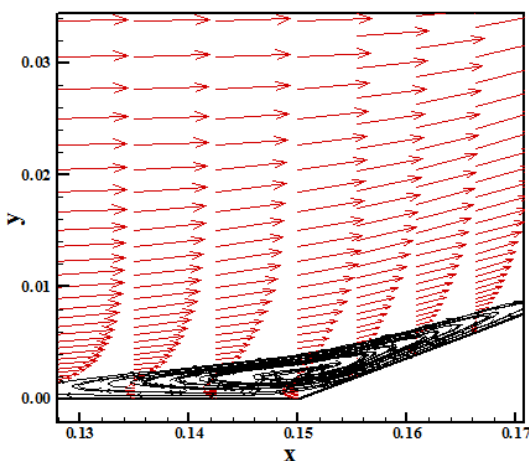


Figure 44. Circulation bubble (LS-CS).

In resume, as can be observed the [9] turbulence model predicts a more energized boundary layer. With it, the weak shock wave ahead of the ramp

corner is negligible and the circulation bubble presents a discrete formation.

**7.2.2 Baldwin and Lomax results/TVD**

In this case, only the [2-4] schemes have presented converged results. Figures 46 to 48 exhibit the pressure contours obtained by the [2-4] schemes, respectively, as using the [10] turbulence model. A weak shock wave is formed ahead of the ramp corner in all solutions. It is important to remember that such weak shock wave is due to the boundary layer detachment which induces a false thick geometry at the ramp and the flow only see this thick geometry, originating the oblique shock wave. So, it is possible to distinguish that the effect of increasing boundary layer thickness is more pronounced in the [4] solution than in the other solutions. It also induces the expected behavior of a larger circulation bubble formed in the [4] solution. In terms of the pressure field, the [2] scheme again presents the most severe pressure field, characterizing this algorithm as more conservative.

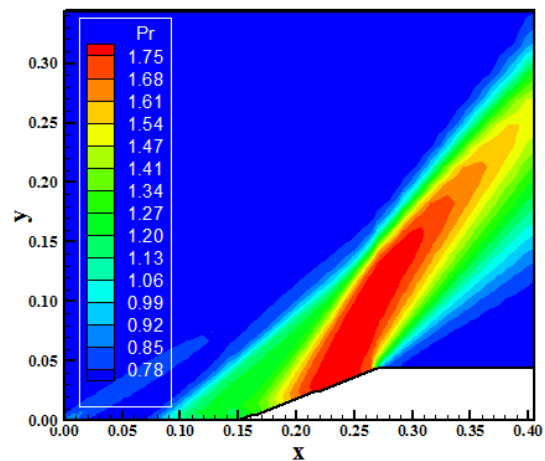


Figure 46. Pressure contours (VL-BL).



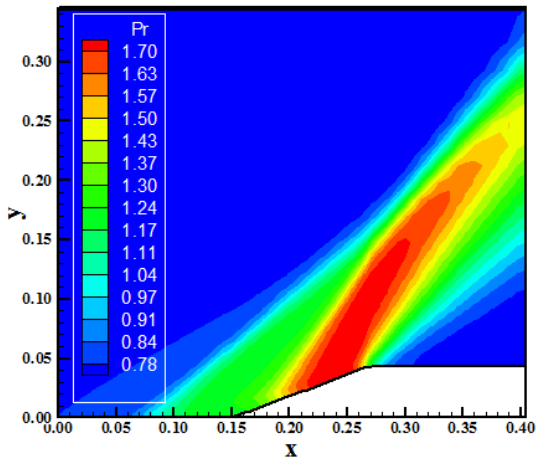


Figure 47. Pressure contours (H-BL).

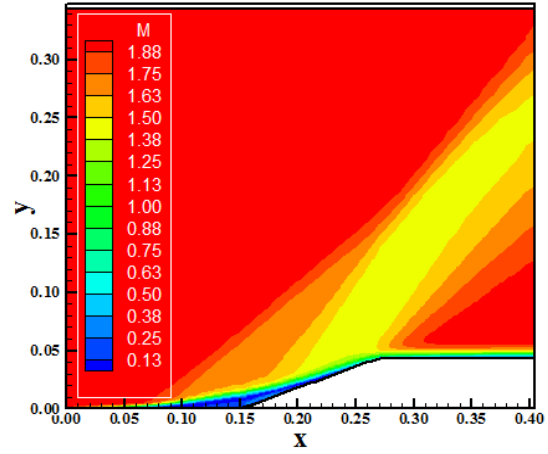


Figure 50. Mach number contours (H-BL).

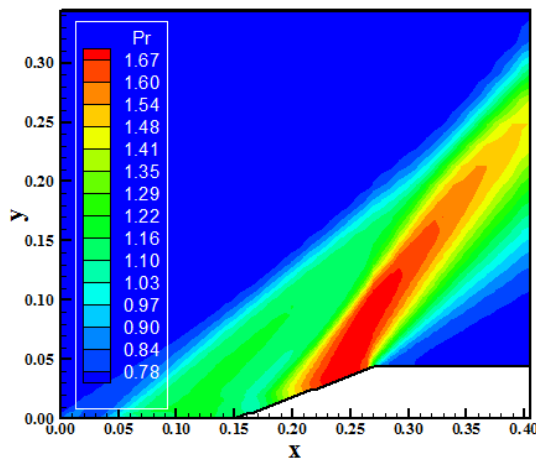


Figure 48. Pressure contours (FPP-BL).

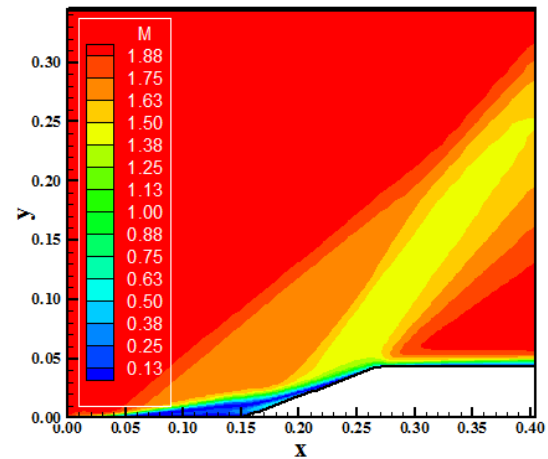


Figure 51. Mach number contours (FPP-BL).

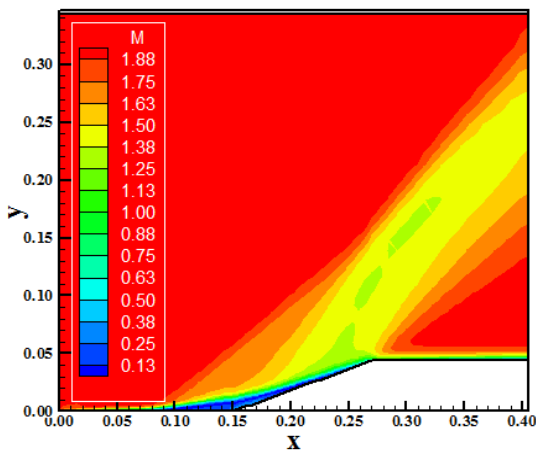


Figure 49. Mach number contours (VL-BL).

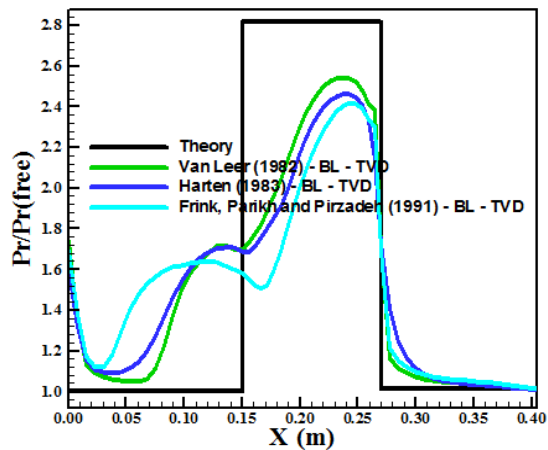


Figure 52. Wall pressure distributions.

Figures 49 to 51 show the Mach number contours obtained by the [2-4] numerical algorithms, respectively, as using the [10] turbulence model. It is possible to observe that the boundary layer

detachment is bigger in the [4] solution, with the consequent formation of a bigger circulation bubble than the other solutions. The Mach number field of all solutions is the same in quantitative terms, although in qualitative terms they are different.

Figure 52 presents the wall pressure distributions generated by all algorithms. As noted, all solutions capture the circulation bubble formation closes to the ramp corner, but all solutions differs from the theoretical solution (all under-predict the shock plateau).

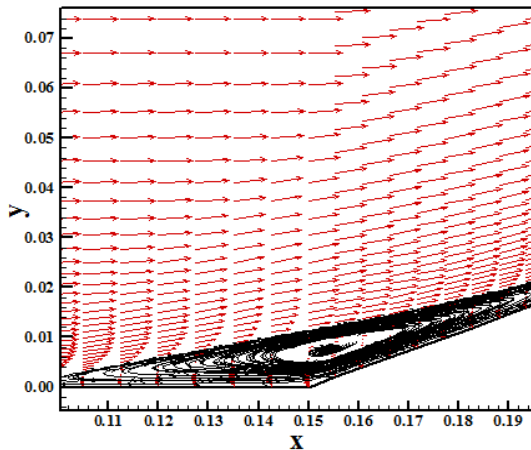


Figure 53. Circulation bubble (VL-BL).

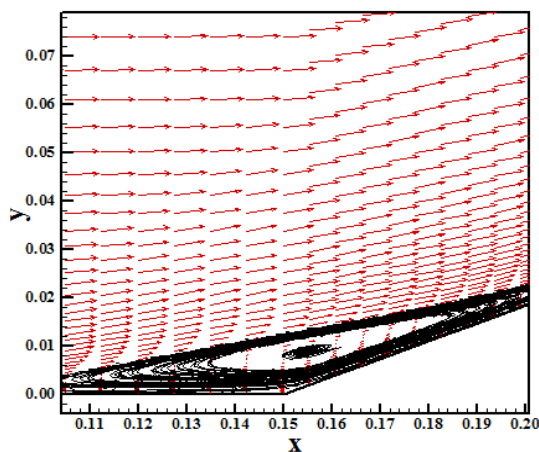


Figure 54. Circulation bubble (H-BL).

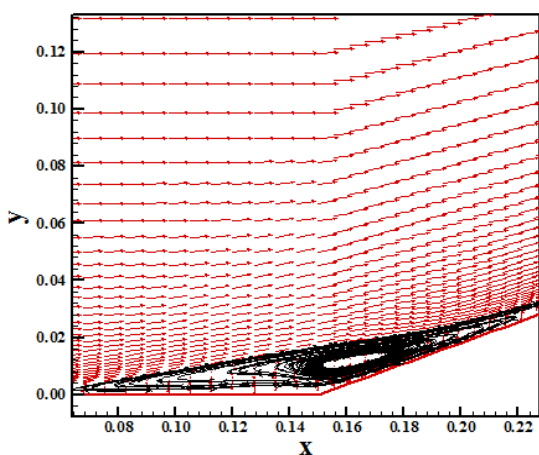


Figure 55. Circulation bubble (FPP-BL).

Figures 53 to 55 exhibit the circulation bubble formed close to the ramp corner generated by the [2-4] algorithms. The [4] schemes present the a bigger circulation bubble extent and size than the others.

In resume, the [10] turbulence model predicts a great extent region of boundary layer detachment and, consequently, bigger bubble size. The [10] model predicts bigger separation than the [9] model.

### 7.2.3 Sparlat and Allmaras results/TVD

Only the [5] scheme did not present converged results. Figures 56 to 59 present the pressure contours obtained by the [2-4,7] schemes, respectively, as using the [11] turbulence model. The [2] solution captures a small boundary layer detachment, which results in a less intense weak shock wave. The [4] solution captures the biggest boundary layer detachment, which results in a more intense weak shock wave. The pressure field generated by the [2] scheme is again the most severe in relation to those generated by the others schemes.

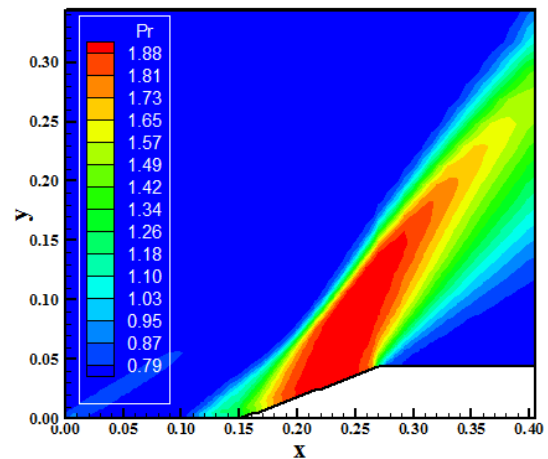


Figure 56. Pressure contours (VL-SA).

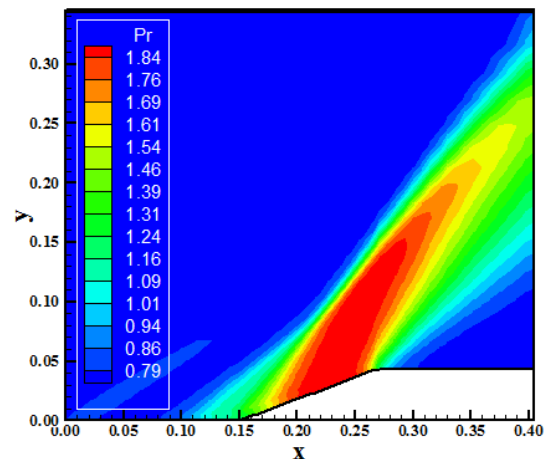


Figure 57. Pressure contours (H-SA).

quantitative terms the solutions are the same, the difference existing in qualitative terms.

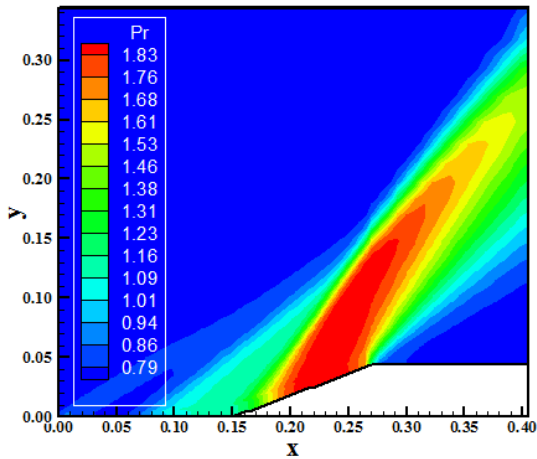


Figure 58. Pressure contours (FPP-SA).

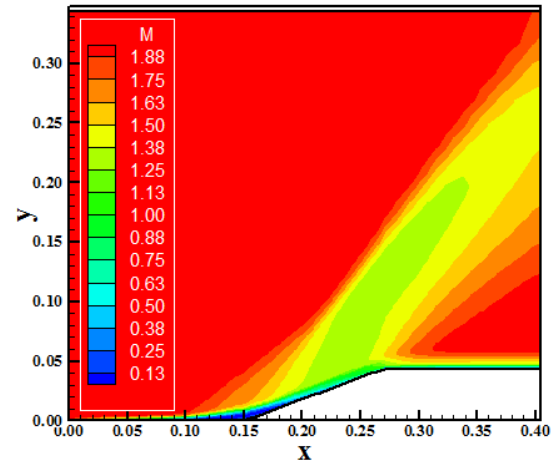


Figure 61. Mach number contours (H-SA).

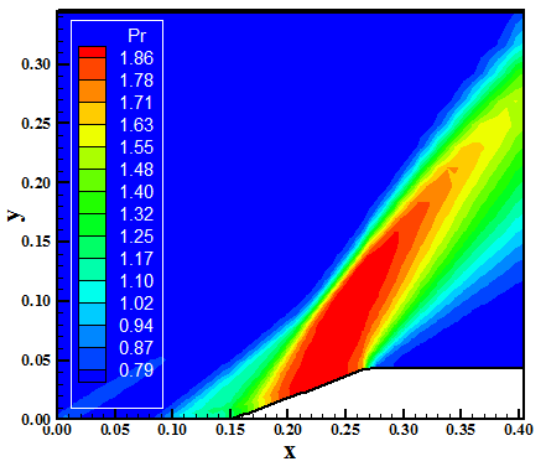


Figure 59. Pressure contours (RK-SA).

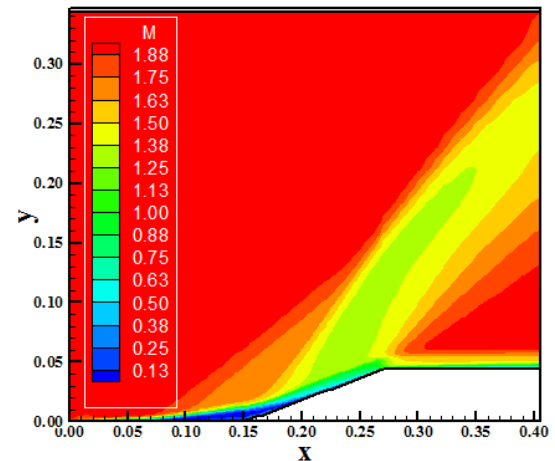


Figure 62. Mach number contours (FPP-SA).

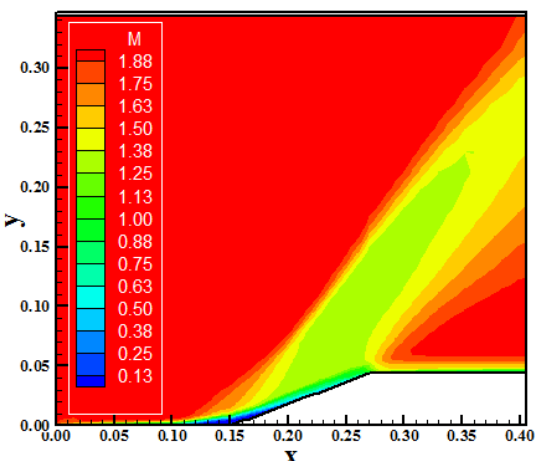


Figure 60. Mach number contours (VL-SA).

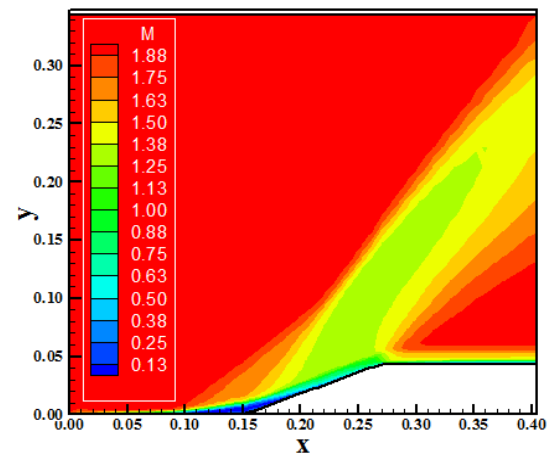


Figure 63. Mach number contours (RK-SA).

Figures 60 to 63 show the Mach number contours obtained by the [2-4,7] numerical schemes, respectively. The [4] solution again captures a bigger circulation bubble than the other solutions. In

Figure 64 shows the wall pressure distributions obtained by the [2-4,7] algorithms. All solutions

capture the circulation bubble at the ramp corner. Moreover, the [2] pressure peak is close to the theoretical pressure plateau.

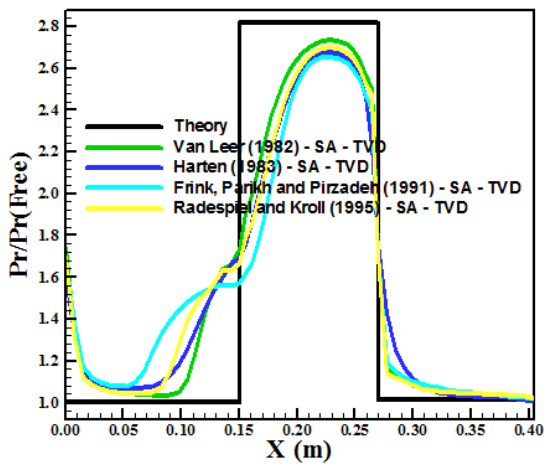


Figure 64. Wall pressure distributions.

It is important to be mentioned here that the best behavior to the pressure plateau was obtained by the [9] turbulence model in spite of the loss of physical meaning of the flow (loss of the circulation bubble formation).

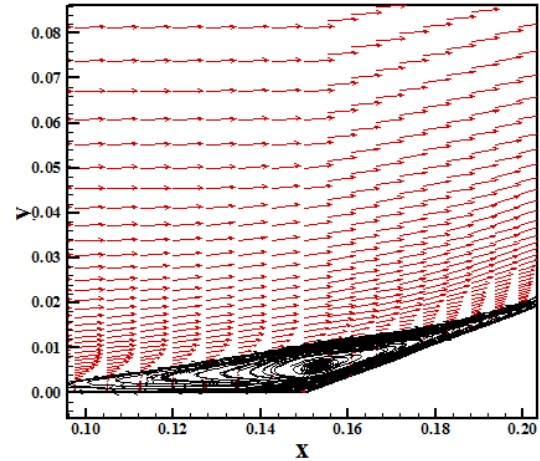


Figure 67. Circulation bubble (FPP-SA).

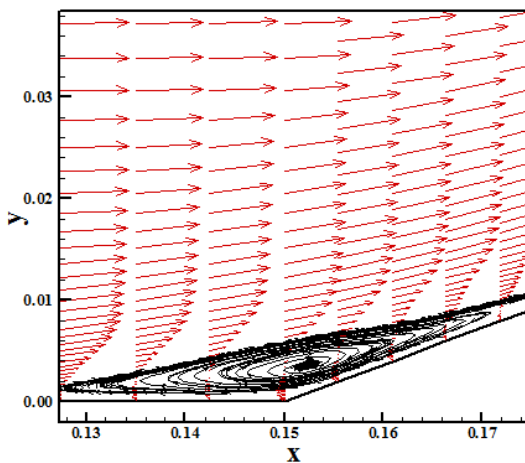


Figure 65. Circulation bubble (VL-SA).

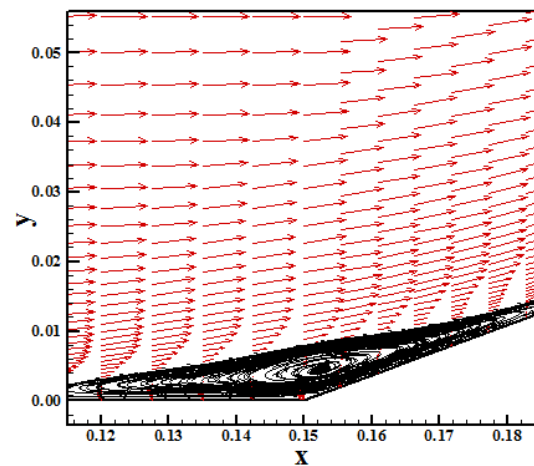


Figure 68. Circulation bubble (RK-SA).

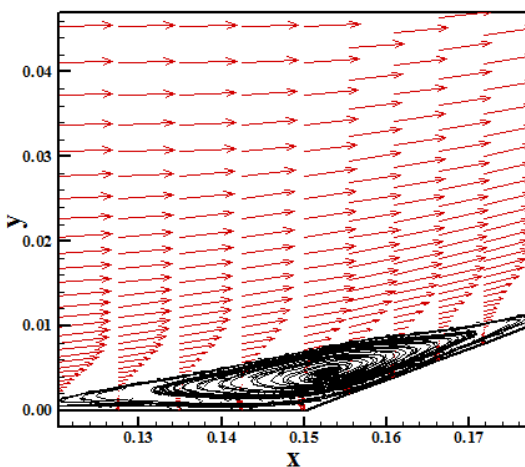


Figure 66. Circulation bubble (H-SA).

Figures 65 to 68 exhibit the circulation bubble captured by the [2-4,7] schemes, respectively, as using the [11] turbulence model. As can be seen, the [4] solution generates the largest bubble region than the other solutions.

In resume, the [11] turbulence model predicts a less extent region of boundary layer detachment and, consequently, minor bubble size. The [11] model, an one-equation model, predicts less severe separation than the [10] model.

### 7.3 Quantitative Analysis

One way to quantitatively verify if the solutions generated by each scheme are satisfactory consists in determining the shock angle of the oblique shock

wave,  $\beta$ , measured in relation to the initial direction of the flow field. [34] (pages 352 and 353) presents a diagram with values of the shock angle,  $\beta$ , to oblique shock waves. The value of this angle is determined as function of the freestream Mach number and of the deflection angle of the flow after the shock wave,  $\phi$ . To  $\phi = 20^\circ$  (ramp inclination angle) and to a freestream Mach number equals to 2.0, it is possible to obtain from this diagram a value to  $\beta$  equals to  $53.0^\circ$ . Using a transfer in Figures 4 to 8 (laminar, first order), Figs. 20 to 22 (laminar, second order), Figs. 30 to 34 (CS), Figs. 46 to 48 (BL), Figs. 56 to 59 (SA), it is possible to obtain the values of  $\beta$  to each scheme and to each studied case, as well the respective errors, shown in Tab. 3.

Table 3. Values of the oblique shock wave angle.

| Case         | Lam.,<br>1 <sup>st</sup> | Lam.,<br>2 <sup>nd</sup> | CS,<br>TVD | BL,<br>TVD | SA,<br>TVD |
|--------------|--------------------------|--------------------------|------------|------------|------------|
| <b>VL</b>    | 51.0                     | 56.4                     | 51.0       | 53.0       | 51.6       |
| <b>Error</b> | 3.77                     | 6.42                     | 3.77       | 0.00       | 2.64       |
| <b>H</b>     | 49.3                     | 55.0                     | 52.5       | 55.0       | 51.7       |
| <b>Error</b> | 6.98                     | 3.77                     | 0.94       | 3.77       | 2.45       |
| <b>FPP</b>   | 52.4                     | 51.6                     | 51.4       | 53.0       | 55.0       |
| <b>Error</b> | 1.13                     | 2.64                     | 3.02       | 0.00       | 3.77       |
| <b>LS</b>    | 53.0                     | -                        | 52.0       | -          | -          |
| <b>Error</b> | 0.00                     | -                        | 1.89       | -          | -          |
| <b>RK</b>    | 51.0                     | -                        | 51.2       | -          | 53.0       |
| <b>Error</b> | 3.77                     | -                        | 3.40       | -          | 0.00       |

It is possible to distinguish that only the [3] scheme did not capture the exact value of the oblique shock wave angle. All other schemes capture this exact value in a particular case. The [10] turbulence model was the most exact because allows the [2] and [4] schemes to capture accurately the shock angle.

Table 4. Computational data.

| Case       | Lam.,<br>1 <sup>st</sup> | Lam.,<br>2 <sup>nd</sup> | CS,<br>TVD | BL,<br>TVD | SA,<br>TVD |
|------------|--------------------------|--------------------------|------------|------------|------------|
| <b>VL</b>  | 0.7 <sup>(1)</sup>       | 0.1                      | 0.1        | 0.1        | 0.1        |
|            | 3,872                    | 32,138                   | 12,318     | 32,144     | 19,961     |
| <b>H</b>   | 0.9 <sup>(1)</sup>       | 0.9                      | 0.9        | 0.9        | 0.9        |
|            | 2,909                    | 3,880                    | 1,100      | 3,880      | 2,376      |
| <b>FPP</b> | 0.9 <sup>(1)</sup>       | 0.1                      | 0.1        | 0.1        | 0.1        |
|            | 6,326                    | 48,378                   | 22,374     | 48,378     | 34,615     |
| <b>LS</b>  | 0.9 <sup>(1)</sup>       | -                        | 0.1        | -          | -          |
|            | 6,484                    | -                        | 22,593     | -          | -          |
| <b>RK</b>  | 0.9 <sup>(1)</sup>       | -                        | 0.1        | -          | 0.1        |
|            | 3,904                    | -                        | 13,614     | -          | 33,091     |

<sup>(1)</sup>: Convergence in 4 orders.

Table 4 presents the computational data of the simulations. With exception of the first order results, all others results converged in three (3) orders. All second order solutions of the [2,4-5,7] scheme converged with a CFL number of 0.1. On the other hand, all second order solutions of the [3] scheme converged with a CFL Number of 0.9. It is important to highlight the excellent convergence of the [3] scheme, converging in all cases with a CFL number of 0.9.

## 8 Conclusions

This work describes five numerical tools to perform perfect gas simulations of the laminar and turbulent viscous flow in two-dimensions. The [2-5,7] schemes, in its first- and second-order versions, are implemented to accomplish the numerical simulations. The Navier-Stokes equations, on a finite volume context and employing structured spatial discretization, are applied to solve the supersonic flow along a ramp in two-dimensions. Three turbulence models are applied to close the system, namely: [9], [10] and [11]. On the one hand, the second-order version of the [2,4-5,7] schemes are obtained from a "MUSCL" extrapolation procedure, whereas on the other hand, the modified flux function approach is applied in the [3] scheme for the same accuracy. The convergence process is accelerated to the steady state condition through a spatially variable time step procedure, which has proved effective gains in terms of computational acceleration (see [18-19]). The results have shown that the [2,4-5,7] schemes have yielded the best results in terms of the prediction of the shock angle at the ramp. Moreover, the wall pressure distribution is also better predicted by the [2] scheme.

It is important to emphasize that the study of the present turbulence models aims a verification of their potentialities to be used in re-entry flows in Earth and entry flows in Mars, to perform turbulent reactive simulations on the future. Some references to the reader become familiar with such line of research of the present author are: [35-39].

### References:

- [1] P. Kutler, Computation of Three-Dimensional, Inviscid Supersonic Flows, *Lecture Notes in Physics*, Vol. 41, 1975, pp. 287-374.
- [2] B. Van Leer, Flux-Vector Splitting for the Euler Equations, *Proceedings of the 8<sup>th</sup> International Conference on Numerical Methods in Fluid Dynamics*, E. Krause, Editor,

- Lecture Notes in Physics, Vol. 170, 1982, pp. 507-512, Springer-Verlag, Berlin.
- [3] A. Harten, High Resolution Schemes for Hyperbolic Conservation Laws, *Journal of Computational Physics*, Vol. 49, 1983, pp. 357-393.
- [4] N. T. Frink, P. Parikh, and S. Pirzadeh, Aerodynamic Analysis of Complex Configurations Using Unstructured Grids, *AIAA 91-3292-CP*, 1991.
- [5] Liou, M., and Steffen Jr., C. J., 1993, A New Flux Splitting Scheme, *Journal of Computational Physics*, Vol. 107, 1993, pp. 23-39.
- [6] P. L. Roe, Approximate Riemann Solvers, Parameter Vectors, and Difference Schemes, *Journal of Computational Physics*, Vol. 43, 1981, pp. 357-372.
- [7] Radespiel, R., and Kroll, N., Accurate Flux Vector Splitting for Shocks and Shear Layers, *Journal of Computational Physics*, Vol. 121, 1995, pp. 66-78.
- [8] C. Hirsch, *Numerical Computation of Internal and External Flows Computational Methods for Inviscid and Viscous Flows*, John Wiley & Sons Ltd, 1990, 691p.
- [9] T. Cebeci, and A. M. O. Smith, A Finite Difference Method for Calculating Compressible Laminar and Turbulent Boundary Layers, *Journal of Basic Engineering*, Trans. ASME, Series B, Vol. 92, No. 3, 1970, pp. 523-535.
- [10] B. D. Baldwin, and H. Lomax, Thin Layer Approximation and Algebraic Model for Separated Turbulent Flows, *AIAA Paper 78-257*, 1978.
- [11] P. R. Sparlat, and S. R. Allmaras, A One-Equation Turbulence Model for Aerodynamic Flows, *AIAA Paper 92-0439*, 1992.
- [12] Secundov, Smirnova, Kozlov, Gulyaev, One-Equation Eddy Viscosity Model (Modified L. S. J. Kovaszny Model), Short Summary of the Equations, *Personal Communication*, 1990.
- [13] Hunt, J. C. R., Turbulence Structure in Thermal Convection and Shear-Free Boundary Layers, *J. Fluid Mech.*, Vol. 138, 1984, pp. 161-184.
- [14] E. S. G. Maciel, and N. G. C. R. Fico Jr., High Resolution Algorithms Coupled with the Baldwin and Lomax Model Applied to a Turbulent Flow Problem, *Proceedings of the 5<sup>th</sup> Spring School of Transition and Turbulence (V EPTT)*, Rio de Janeiro, RJ, Brazil, 2006. [available in CD-ROM]
- [15] E. S. G. Maciel, First Order Upwind Algorithms Coupled with the Baldwin and Lomax Model Applied to Turbulent Flow Problems – Part II, *Proceedings of the V National Congress of Mechanical Engineering (V CONEM)*, Salvador, BA, Brazil, 2008. [available in CD-ROM]
- [16] E. S. G. Maciel, Comparison Between the Cebeci and Smith and the Baldwin and Lomax Turbulence Models – Final Results, *Proceedings of the VI National Congress of Mechanical Engineering (VI CONEM)*, Campina Grande, PB, Brazil, 2010. [available in CD-ROM]
- [17] A. Jameson, and D. J. Mavriplis, Finite Volume Solution of the Two-Dimensional Euler Equations on a Regular Triangular Mesh, *AIAA Journal*, Vol. 24, No. 4, 1986, pp. 611-618.
- [18] E. S. G. Maciel, Analysis of Convergence Acceleration Techniques Used in Unstructured Algorithms in the Solution of Aeronautical Problems – Part I, *Proceedings of the XVIII International Congress of Mechanical Engineering (XVIII COBEM)*, Ouro Preto, MG, Brazil, 2005. [available in CD-ROM]
- [19] E. S. G. Maciel, Analysis of Convergence Acceleration Techniques Used in Unstructured Algorithms in the Solution of Aerospace Problems – Part II”, *Proceedings of the XII Brazilian Congress of Thermal Engineering and Sciences (XII ENCIT)*, Belo Horizonte, MG, Brazil, 2008. [available in CD-ROM]
- [20] R. W. Fox, and A. T. McDonald, *Introdução à Mecânica dos Fluidos*, Ed. Guanabara Koogan, Rio de Janeiro, RJ, Brazil, 632p, 1988.
- [21] E. S. G. Maciel, Comparison Among the First Order Upwind Algorithms of Roe, of Steger and Warming, of Van Leer and of Chakravarthy and Osher in the Solution of the Euler Equations in 2D – Theory, *Proceedings of the VIII Symposium of Computational Mechanics (VIII SIMMEC)*, Belo Horizonte, MG, Brazil, 2008. [available in CD-ROM]
- [22] E. S. G. Maciel, Comparison Among the First Order Upwind Algorithms of Roe, of Steger and Warming, of Van Leer and of Chakravarthy and Osher in the Solution of the Euler Equations in 2D – Results, *Proceedings of the VIII Symposium of Computational Mechanics (VIII SIMMEC)*, Belo Horizonte, MG, Brazil, 2008. [available in CD-ROM]
- [23] E. S. G. Maciel, Comparação entre Algoritmos de Separação de Vetores de Fluxo e de Diferenças de Fluxo de Primeira Ordem na

Solução das Equações de Euler em Duas Dimensões Teoria, *Proceedings of the Primer Congreso Argentino Ingeniería (I CAIM)*, Bahía Blanca, Argentina, 2008. [available in CD-ROM]

- [24] E. S. G. Maciel, Comparação entre Algoritmos de Separação de Vetores de Fluxo e de Diferenças de Fluxo de Primeira Ordem na Solução das Equações de Euler em Duas Dimensões – Resultados Finais, *Proceedings of the Primer Congreso Argentino Ingeniería (I CAIM)*, Bahía Blanca, Argentina, 2008. [available in CD-ROM]
- [25] E. S. G. Maciel, Comparison Among Predictor-Corrector, Symmetrical and TVD Upwind Schemes in the Solution of the Euler Equations in Two-Dimensions – Theory, *Proceedings of the 19<sup>th</sup> International Congress of Mechanical Engineering (XIX COBEM)*, Brasília, DF, Brazil, 2007. [available in CD-ROM]
- [26] E. S. G. Maciel, Comparison Among Predictor-Corrector, Symmetrical and TVD Upwind Schemes in the Solution of the Euler Equations in Two-Dimensions – Results, *Proceedings of the 19<sup>th</sup> International Congress of Mechanical Engineering (XIX COBEM)*, Brasília, DF, Brazil, 2007. [available in CD-ROM]
- [27] E. S. G. Maciel, Extension of the Steger and Warming and Radespiel and Kroll Algorithms to Second Order Accuracy and Implicit Formulation Applied to the Euler Equations in Two-Dimension Theory, *Proceedings of the VI National Congress of Mechanical Engineering (VI CONEM)*, Campina Grande, Paraíba, Brazil, 2010. [available in CD-ROM]
- [28] E. S. G. Maciel, Extension of the Steger and Warming and Radespiel and Kroll Algorithms to Second Order Accuracy and Implicit Formulation Applied to the Euler Equations in Two-Dimension Results, *Proceedings of the VI National Congress of Mechanical Engineering (VI CONEM)*, Campina Grande, Paraíba, Brazil, 2010. [available in CD-ROM]
- [29] E. S. G. Maciel, Extension of the Roe and Van Leer Algorithms to Second Order Accuracy Applied to the Euler Equations in Two-Dimensions, *Proceedings of the 12th Pan-American Congress of Applied Mechanics (XII PACAM)*, Port of Spain, Trinidad, 2012. [available in CD-ROM]
- [30] E. S. G. Maciel, Extension of the Frink, Parikh and Pirzadeh and Liou and Steffen Jr. Algorithms to Second Order Accuracy and Implicit Formulations Applied to the Euler Equations in Two-Dimensions Theory, *Proceedings of the VII National Congress of Mechanical Engineering (VII CONEM)*, São Luis do Maranhão, Maranhão, Brazil, 2012. [available in CD-ROM]
- [31] E. S. G. Maciel, Extension of the Frink, Parikh and Pirzadeh and Liou and Steffen Jr. Algorithms to Second Order Accuracy and Implicit Formulations Applied to the Euler Equations in Two-Dimensions Results, *Proceedings of the VII National Congress of Mechanical Engineering (VII CONEM)*, São Luis do Maranhão, Maranhão, Brazil, 2012. [available in CD-ROM]
- [32] D. J. Mavriplis, and A. Jameson, Multigrid Solution of the Navier-Stokes Equations on Triangular Meshes, *AIAA Journal*, Vol. 28, 1990, No. 8, pp. 1415-1425.
- [33] E. S. G. Maciel, Simulação Numérica de Escoamentos Supersônicos e Hipersônicos Utilizando Técnicas de Dinâmica dos Fluidos Computacional, *Doctoral Thesis, ITA, CTA*, São José dos Campos, SP, Brazil, 2002.
- [34] J. D. Anderson Jr., *Fundamentals of Aerodynamics*, McGraw-Hill, Inc., EUA, 1984, 563p.
- [35] E. S. G. Maciel, and A. P. Pimenta, Thermochemical Non-Equilibrium Reentry Flows in Two-Dimensions – Part I, *WSEAS Transactions on Mathematics*, Vol. 11, Issue 6, June, 2012, pp. 520-545.
- [36] E. S. G. Maciel, and A. P. Pimenta, Thermochemical Non-Equilibrium Reentry Flows in Two-Dimensions – Part II, *WSEAS Transactions on Mathematics*, Vol. 11, Issue 11, November, 2012, pp. 977-1005.
- [37] E. S. G. Maciel, and A. P. Pimenta, Thermochemical Non-Equilibrium Reentry Flows in Two-Dimensions: Seven Species Model – Part I, *WSEAS Transactions on Applied and Theoretical Mechanics*, Vol. 7, Issue 4, October, 2012, pp. 311-337.
- [38] E. S. G. Maciel, and A. P. Pimenta, Thermochemical Non-Equilibrium Reentry Flows in Two-Dimensions: Seven Species Model – Part II, *WSEAS Transactions on Applied and Theoretical Mechanics*, Vol. 8, Issue 1, January, 2013, pp. 55-83.
- [39] E. S. G. Maciel, and A. P. Pimenta, Thermochemical Non-Equilibrium Entry Flows in Mars in Two-Dimensions – Part I, *WSEAS Transactions on Applied and Theoretical Mechanics*, Vol. 8, Issue 1, January, 2013, pp. 26-54.